ADAPTING EARLY TRANSITION METAL AND NON-METALLIC DOPANTS ON COBALT-BASED OXYHYDROXIDES FOR ENHANCED ALKALINE AND NEUTRAL SALINE WATER OXIDATION

An Undergraduate Research Scholars Thesis

by

AHMED MOHAMED[1], EBTIHAL YOUSSEF[2], FATMA AHMED[3], HANIA ELSAYED[4], AND RANA MOHSEN[5]

Submitted to the LAUNCH: Undergraduate Research office at
Texas A&M University
in partial fulfillment of requirements for the designation as an

UNDERGRADUATE RESEARCH SCHOLAR

Approved by
Faculty Research Advisor: Dr. Ahmed Abdel-Wahab

May 2021

Majors: Chemical Engineering[1, 2, 3, 4, 5]

RESEARCH COMPLIANCE CERTIFICATION

Research activities involving the use of human subjects, vertebrate animals, and/or biohazards must be reviewed and approved by the appropriate Texas A&M University regulatory research committee (i.e., IRB, IACUC, IBC) before the activity can commence. This requirement applies to activities conducted at Texas A&M and to activities conducted at non-Texas A&M facilities or institutions. In both cases, students are responsible for working with the relevant Texas A&M research compliance program to ensure and document that all Texas A&M compliance obligations are met before the study begins.

We, Ahmed Mohamed[1], Ebtihal Youssef[2], Fatma Ahmed[3], Hania Elsayed[4], and Rana Mohsen[5] , certify that all research compliance requirements related to this Undergraduate Research Scholars thesis have been addressed with my Research Faculty Advisor prior to the collection of any data used in this final thesis submission.

This project did not require approval from the Texas A&M University Research Compliance & Biosafety office.

TABLE OF CONTENTS

ABSTRACT

Adapting Early Transition Metal and Non-Metallic Dopants on Cobalt-Based Oxyhydroxides for Enhanced Alkaline and Neutral Saline Water Oxidation

Ahmed Mohamed[1], Ebtihal Youssef[2], Fatma Ahmed[3], Hania Elsayed[4], and Rana Mohsen[5]
Department of Chemical Engineering[1]
Department of Chemical Engineering[2]
Department of Chemical Engineering[3]
Department of Chemical Engineering[4]
Department of Chemical Engineering[5]
Texas A&M University

Research Faculty Advisor: Ahmed Abdel-Wahab
Department of Chemical Engineering
Texas A&M University

The sluggish oxygen evolution reaction (OER) has been a major barrier for advancing green hydrogen production from water splitting. Whilst the overwhelming majority of work has been devoted towards buffered pure water electrolytes, a growing interest in the field is now emerging towards utilizing buffered seawater as a natural electrolyte feed to the electrolyzer. Investigation of highly electro-active, stable, cost-effective, and earth-abundant electrocatalysts in saline electrolytes is seen as a prerequisite to the commercial realization of saline water electrolysis.

We undertook the design challenge of the electrocatalysts to be developed by rationally integrating key features that have been proven detrimental to both activity and stability of anodic materials in water electrolysis. In doing so, we initially fabricated crystalline spinel Co_3O_4 through the highly scalable solution combustion synthesis (SCS) to act as the catalyst's core and

Co-source. The highly crystalline core acts as a conductive substrate and serves as a template for growing the active electrochemical surface area. Further, we developed highly modulated S,B-(CoFeCr) and S,B-(CoFeV) oxyhydroxide shells atop the spinel core, with a high ratio of surface Co^{2+}. Non-metallic dopants were employed to both synergistically enhance activity through surface modulation and offer a highly hydrophilic surface that activates higher performance during near-neutral water oxidation – when H_2O adsorption is the initial OER step.

We performed an array of surface chemistry and textural characterization techniques including HRTEM, FESEM, EDS, XRD, Elemental Mapping, and Raman spectroscopy to effectively investigate the highly active catalysts developed. Pre- and post-OER XPS analyses were undertaken to reveal the changes in surface chemistry of the attained oxyhydroxides after prolonged OER operation. The as-prepared S,B-(CoFeCr)OOH and S,B-(CoFeV)OOH electrocatalysts deposited on glassy carbon electrodes (GCE) required low overpotentials of 174 and 242 mV to achieve current density of 10 mA cm^{-2}, respectively, in alkaline saline (1M KOH + 0.5M NaCl) electrolyte, with low Tafel slopes of 45.3 and 51.2 mV dec^{-1}. The reported materials are amongst the most active based on our literature survey and have exhibited high stabilities in harsh electrolytic regimes.

Moreover, we attained polarization curves for these electrocatalysts in near-neutral pH (1M HCO_3^-/CO_3^{2-} + 0.6M NaCl; pH = 8) and neutral pH (1M PB + 0.6M NaCl; pH = 7) saline electrolytes. Chronoamperometry (CA) studies were performed in neutral saline electrolytes in order to ensure chlorine corrosion resistance and quantify chlorine evolution reaction (CER) products. To attain higher performance and more accurately test for stabilities in realistic seawater mimicking environments, the optimum trimetallic oxyhydroxides were deposited on conductive and highly porous nickel foam (NF). S,B-(CoFeCr)OOH@NF and S,B-

(CoFeV)OOH@NF achieved 50 hours of chronopotentiometric stabilities under neutral saline electrolyte and 1.71 V (vs. RHE) of applied potential. Further, the materials exhibited suppressed CER products formation rates of 0.014 and 0.044 mg $(Lh)^{-1}$, respectively, for the Cr and V doped oxyhydroxides. We correlate the higher CER suppression of the Cr analogue to stronger localized $Cr^{\delta+}(OOH)^{\delta-}$ which activates stronger electrostatic shielding from anionic Cl^- and aids in H_2O dissociation kinetics at neutral pH operation. This study provides a systematic approach towards a rational design of highly active and stable electrocatalysts.

ACKNOWLEDGEMENTS

Contributors

We would like to thank our faculty advisor, Dr. Ahmed Abdel-Wahab, and our lab advisor, PhD. Candidate Ahmed Badreldin, for their guidance and support throughout the course of this research. Thanks also goes to our friends, colleagues, the department faculty and staff for making our time at Texas A&M University a great experience. Finally, thanks to our family for their encouragement and to our family for their patience and love.

The materials synthesis, electrochemical experiments, and initial data analysis for Adapting Early Transition Metal and Non-Metallic Dopants on cobalt-based Oxyhydroxides for Enhanced Alkaline and Neutral Saline Water Oxidation were performed by Ahmed Mohamed, Ebtihal Youssef, Fatma Ahmed, Hania Elsayed, Rana Mohsen and Noor Mubarak, under the day-to-day mentorship of Ahmed Badreldin and supervision of Dr. Ahmed Abdel-Wahab. The materials characterization was conducted in part by the Chemical Engineering Program laboratories and in part by the Central Materials Characterization laboratory at Texas A&M University at Qatar. These data are unpublished during the time of submitting this thesis. All other work conducted for the thesis was completed by the students independently.

Funding Sources

This undergraduate research was supported by the Chemical Engineering Program at Texas A&M University at Qatar. This work was also made possible in part by a grant from the Qatar National Research Fund under its National Priorities Research Program under Grant Number NPRP12S-0131-190024 and by Qatar Shell Research and Technology Center (QSRTC).

Its contents are solely the responsibility of the authors and do not necessarily represent the official views of the Qatar National Research Fund.

1. INTRODUCTION

Hydrogen produced from water electrolysis using generated electricity from renewable sources of energy is envisaged to be the fuel of the future. There have been concerted efforts worldwide towards the transition to a hydrogen economy[1-4]. The present and foreseeable decrease in the cost of renewable energy, such as solar, wind, and geothermal, will result in the propagating reduction in costs pertaining to green hydrogen generation through water electrolysis. This highlights the importance of developing highly stable electrocatalysts that can efficiently and reliably produce oxygen for extended periods at industrial scale current densities[5]. The electrocatalysis of water splitting consists of the cathodic hydrogen evolution reaction (HER, acidic medium: $2H^+ + 2e^- \rightarrow H_2$, neutral and alkaline medium: $2H_2O + 2e^- \rightarrow H_2 + 2OH^-$) and anodic oxygen evolution reaction (OER, acidic and neutral medium: $2H_2O \rightarrow O_2 + 4H^+ + 4e^-$, alkaline medium $4OH^- \rightarrow 2H_2O + O_2 + 4e^-$). The OER reaction is more thermodynamically favorable, yet it is kinetically sluggish because of the four-electron transfer scheme in the mechanism. The utilization of electrocatalytic means for generating an abundant supply of green hydrogen can best be commercially and industrially realized if direct saline/seawater is employed as feed to the electrolyzer. This strategy has been widely promoted due to the limited fresh water resources in regions where renewable energy sources (e.g., solar) are abundant, and the fact that seawater is a natural electrolyte. Nonetheless, limited efforts have been dedicated to investigating potential electrocatalytic candidates for both the cathodic and anodic reactions in saline/seawater media. Further, the stability of the O–O intermediates propose a challenge since the presence of chloride (Cl^-) ions which pose lower kinetic hinderances due to the facile two electron transfer mechanism in generation of chloro-reaction products [6]. Up until recently, RuO_2 and IrO_2 based

catalysts were the benchmarks for the OER because of their high activity. However, their scarcity, and consequently high cost and poor stability and selectivity in saline conditions limit their applicability[7]. In particular, the formation of the perox group with O_{cus} atom on neighboring Ru atoms can act as active sites for the anodically undesired chlorine evolution reaction (CER) relative to the desired OER[8]. Albeit chloro-reaction products from CER have a market, their toxic nature (i.e., hypochlorite, chlorite, chlorate, chlorine) and additional cost of separation cap their desire of production in saline water electrolysis applications aimed towards hydrogen production. Nickel–iron composite deposited on macroporous nickel foam substrates, NiFe-hydroxide/NF, which is a Nickel–iron composite deposited on macroporous nickel foam substrates was reported to exhibit higher performances and stabilities without the limitations of conventional IrO_2 and RuO_2 anodic electrocatalysts[9]. This motivates exploring different groups like earth-abundant transition metals-based oxides[9-12], nitrides[13], sulfides[14, 15], phosphides[16], and borides[17, 18] as possible alternatives to noble metal-based materials. Recent developments on oxyhydroxides showed promising results with ultra-low overpotential, high durability and cost-effective materials.

As recently reported by Dionigi et al., NiFe-based oxyhydroxides synthesized through, showed promising results of high durability and activity. Low overpotentials of 206 mV at a current density of 10 mA cm^{-2} in non-saline alkaline (1M KOH) electrolyte were reported using NiFe-rGO LDH hybrid catalyst[19]. Some hierarchal sulfides and nitrides are also showing promising results due to their innate electrochemical stabilities in saline water as a result of high electroactivities ,and stabilities possibly from shielding against chloride corrosion[20,21]. Recent developments incorporated cobalt-based electrocatalysts due to favorable energetics on the cobalt surfaces for alkaline and near-neutral OER[22]. Furthermore, a recent report showed that modifying the substrate structure improved performance as a result of the optimized synergistic

effects. for instance, a 3D cobalt CoFeOOH@CO_2P/NF heterostructure showed an excellent activity whereby an overpotential of 199 mV was enough to achieve a current density of 30 mA/cm^2 in alkaline conditions which was attributed to the hierarchical structures and synergistic effects[23]. Contemporary oxyhydroxides proved capable of surpassing some aspects of the industrial application criteria as was reported by Zhou et al., whereby amorphous mesoporous Ni/Fe(oxy)hydroxide electrocatalysts were fabricated and maintained a high current densities of 500 and 1000 mA cm^{-2} at overpotentials of 259 mV and 289 mV in non-saline alkaline conditions, respectively. The as-prepared catalyst exhibited excellent durability at 500, and 1500 mA cm^{-2} for at least 35 hours[24]. Wang et al. prepared a Sulfur-doped NiFe Oxyhydroxides porous nanoclusters which showed promising results, producing a current density of 1 A cm^{-2} at an overpotential of 260 mV in 1 M KOH electrolyte[25]. The effect of the wet synthesis method's reaction time on the activity was reported and optimized whereby a 2-hour reaction time gave the largest ECSA and consequently highest performance. It was found that sulfur doping improved the hydrophilicity of the electrocatalysts. This sulfur-doped material also showed long term durability, whereby it maintained its catalytic activity at a current density of 1A/cm^2 for at least 50 hours[25]. While the results seem promising, the selectivity of the catalyst towards OER over CER was not discussed since testing was not investigated by Wang et al. Furthermore, boron doping of CoFe oxide was reported to improve the activity of the electrocatalyst. Gupta et al. used B-doped CoFe oxide electrocatalyst in alkaline saline electrolyte and reported overpotentials of 294 and 434 mV at current densities of 10 and 100 mA cm^{-2}, respectively, as well as stable performance [17]. Also, a low Tafel slope value of 52 ±0.4 mV/dec was attained for the optimized material in the same study by Gupta et al., indicating favorable kinetics in alkaline saline media. The higher activity was attributed to the incorporation of Fe and presence of a

boron rich shell which assists in the formation of active CoOOH species on the surface. However, low activity was reported in neutral pH conditions. Similarly, and of motivation to this work, a bi-metallic phospho-boride catalyst (Co-Mo-PB) was reported to improve the catalytic properties of Co-based catalysts, whereby a mere 195 mV overpotential was required to achieve 100 mA cm^{-2} of current density in alkaline water electrolyte. This co-doping strategy was attributed to changing the electron density of the Co atom and yielding highly active CoOOH species, which resulted in improved performance[18]. Furthermore, chromium doped CoFe was reported to produce a current density of 10 mA cm^{-2} when an overpotential of 230 mV was applied. regulatory effect of of chromium in maintaining the Co at lower oxidation valence state was reported to improve catalytic activity[6]. Similarly, vanadium doping on CoFe was reported to yield a current density of 10 mA cm^{-2} at an overpotential of 318 mV due to its electron withdrawing effect which enhances the water oxidation reaction [26]. Early transition metals were shown to improve the Co surface by facilitating the Co^{3+}/Co^{4+} cycling to lower valence Co^{2+}/Co^{3+} which has been reported to lower the overpotential for OER [27, 28].

Seawater represents 96.5% of the total water reservoir[29] and therefore, it provides an inexhaustible water source as feed to the electrolyzer. However, this would require design of catalysts and electrolyzers that can overcome the challenges associated with seawater utilization for water electrolysis, notably CER and corrosion potential. Pertaining to alkaline seawater, the Pourbaix diagram presents the so called *alkaline design criteria*, conveying that 100% selective thermodynamic possibility of the OER is ensured in the pH range of pH~7.5-14, whereby an overpotential less than ~480mV would not result in any CER [30]. Another challenge associated with alkaline seawater electrolysis is the formation of insoluble $Ca^{2+}$and Mg^{2+} hydroxides that can deposit on the surface of electrodes e and membrane dividers in conventional electrolyzers,

blocking the electrochemically active surface area (ECSA) of the cathode and fouling the membranes. This in turn increases overpotentials and consequently increases operational costs of the electrolyzer[31]. This issue can be ameliorated by simply operating under near-neutral pH where the molecular feed species for both OER and HER is predominantly H_2O. Neutral and near neutral pH operation would be advantageous for seawater electrolysis not only to avoid precipitation of Ca and Mg salts, but also to avoid the use of high concentrations of electrolytes, since seawater is a natural electrolyte. It will only require small concentration of pH buffer such as phosphate, bicarbonate, or borate buffers. Moreover, operating the electrolyzer at near neutral pH in more environmentally benign and safer than the extreme acidic or alkaline media. Nevertheless, under the constraints of the Pourbaix diagram, the overpotential window for the thermodynamically selective OER decreases as the local pH at the anode surface decreases below pH7.5. This expounds the OER selectivity challenge when operating the electrolyzer at an ideal neutral pH buffered environment.

The kinetics of OER are sluggish at neutral pH due to the requirement of an additional water dissociation step relative to buffered alkaline conditions. This results in the requirement of high overpotentials and suffers from the economically unfeasible low current densities, and durability for prolonged operation. This requires developing electrocatalysts that are highly active and stable in near-neutral water operation [32]. If near-neutral pH operation is ensured in direct seawater electrolysis, this would ameliorate prohibitively expensive buffers in alkaline conditions and eliminate the requirement of costly pretreatment, desalination, and deionization processes of seawater prior to electrolysis. For neutral or near-neutral pH seawater electrolysis, it is important to use an appropriate pH buffer capable of attaining facile protonation-deprotonation reactions to lower risk of significant local pH drops near the anode, which are consequential

towards CER thermodynamics [68,69]. To this end, we chose the buffers based on suitable pK_a values under which the buffering capacity is maximized; when the pH of the electrolyte approaches the pK_a of the buffer[33].

Herein, we use solution combustion synthesis (SCS) to initially fabricate a cobalt oxide core in a scalable and timely scheme, whereby the Co_3O_4 crystalline cores also serves as the surface Co source. The value of the SCS presents itself in the large-scale production potential with minimal costs compared to expensive precursors and pressure vessels – as would be the case with methods such as the commonly used hydrothermal/solvothermal. We then aim to create an electroactive amorphous shell structure of S,B-codoped CoFe active sites, containing additional doping of an early transition metal (ETM – i.e., Cr or V). This was achieved through treating the Co_3O_4 cores in an environmentally benign single-step wet chemical synthesis. In addition to characterizing the performance of the catalysts in near neutral pH conditions, we have examined the electrochemical performance of the fabricated materials in saline alkaline electrolyte to allow for a wide-net performance comparison with literature. As such, we investigated performances in saline bicarbonate (1M $KHCO_3$ + 0.6M NaCl; pH ~ 8 ±0.1) and neutral pH saline (1M Phosphate Buffer + 0.6M NaCl; pH = ~ 7 ±0.1) systems mimicking the pH range of real seawater. We have also performed CER products quantification using the DPD (N, N-diethyl-p-phenylenediamine) method for hypochlorous acid (in neutral pH conditions) to determine the OER selectivity of the developed catalysts. Lastly, we have tested the effect of metallic substrate by drop-casting the optimum catalyst on pretreated nickel foam (NF) and conducted CA studies in neutral saline electrolyte to qualitatively probe CER suppression and sustained activities in realistic electrolytes. In this work, we utilized different characterization techniques including X-ray photoelectron spectroscopy (XPS), X-ray diffraction (XRD), high-

resolution transmission electron microscopy (HRTEM), field-emission scanning electron microscopy (FESEM), energy-dispersive spectroscopy (EDS), and Raman spectroscopy in order to thoroughly investigate the drivers towards performance and selectivity enhancement of our optimum catalysts for the emergent and crucial field of seawater electrolysis.

2. EXPERIMENTAL SECTION

2.1 Chemicals and Materials

Potassium hydroxide (KOH), cobalt acetate ($Co(CH_3CO_2)_2$), chromium (III) nitrate nonahydrate ($Cr(NO_3)_3•9H_2O$), ammonium metavanadate (NH_4VO_3), iron (II) nitrate nonahydrate ($Fe(NO_3)_2•9H_2O$), glycine ($C_2H_5NO_2$), isopropyl alcohol (C_3H_8O), and cobalt (II) nitrate hexahydrate ($Co(NO_3)_2•6H_2O$) were acquired from Sigma-Aldrich. Sodium borohydride ($NaBH_4$) along with sodium thiosulfate pentahydrate ($Na_2S_2O_3•5H_2O$) were acquired from Alfa Aesar. To obtain the required molar concentrations of electrolyte solutions, deionized water (Millipore (18.2 MΩcm)) was used to dissolve the respective salts.

2.2 Preparation of S,B-CoFe(ETM)OOH Oxyhydroxides

The utilization of solution combustion synthesis (SCS) took place when preparing the core cobalt oxides undergoing a fast single-step synthesis. Briefly, $Co(NO_3)_2•9H_2O$ was dissolved in deionized water where glycine was added while stirring the solution on a hot plate (110 °C) until the aqueous phase nearly dried out. What was left of the aqueous phase 'slug' combusts spontaneously producing spinel Co_3O_4 nanoparticles. The yielded catalyst powder was left to cool in the reaction beaker. A programmable muffle furnace was then employed at a temperature of 800°C for a duration of 5 hours to calcinate the obtained catalyst powder. A runaway reaction was prevented due to the optimum molar ratio of glycine to nitrate salt used which was 3:1.

Preparing S-(CoFeCr)OOH was done by the addition of spinel cobalt oxide (Co_3O_4; 500mg), obtained from the SCS, to a 10 mL solution of $Fe(NO_3)_2•9H_2O$, $Cr(NO_3)_3•9H_2O$,

$Na_2S_2O_3$•$5H_2O$, in an amount such that the molar concentration of Fe to Cr is 2:1, Fe to S_2 is 7:1, and Co to Fe is 14:1 (optimum ratio). This was followed by addition of 8 drops of 1M KOH adjusting the solution to a pH of 10.5. The solution underwent ambient mixing for 10 minutes followed by vacuum filtration and air drying to yield the S-doped ternary oxyhydroxides. A similar procedure was done for the preparation of S-(CoFeV)OOH where the ratio of Fe to V was found to be optimum at 1:1, using NH_4VO_3 as the vanadium salt. The same procedure was repeated for the preparation of S,B-(CoFeV)OOH and S,B-(CoFeCr)OOH; along with the addition of 1 g of $NaBH_4$ as the boron source during dopant precursor mixing. The solution was tip-sonicated for 30 seconds then underwent 20 hours of static conditions to ensure complete $NaBH_4$ reduction and boronation. Again, this was followed by vacuum filtration to collect the samples which were left to air dry overnight in a desiccator. Scheme 1 below summarizes the synthesis of both the S- and S,B-codoped oxyhydroxides.

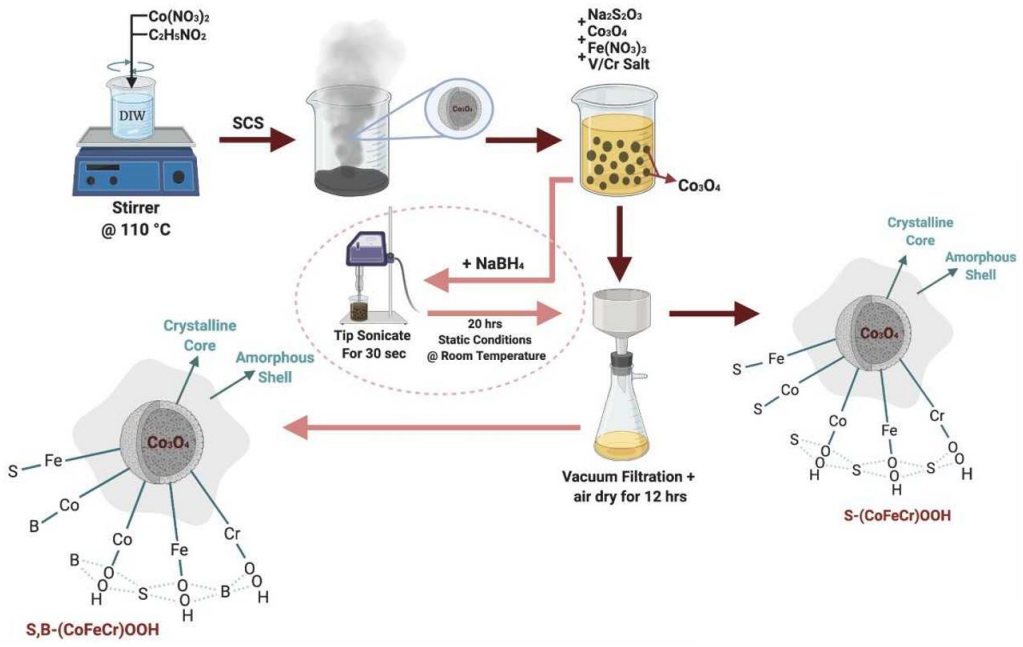

Scheme 1. Synthesis strategy of S- and S,B-codoped CoFe(ETM) ternary oxyhydroxides

2.3 Material Characterization

To obtain quantitative information on the top 1-10 nm electroactive surface, an AXIS Ultra DLD X-ray Photoelectron Spectroscope (XPS) was used. The device is applied to collect high-resolution spectra of S- doped and S,B- codoped CoFe(ETM) oxyhydroxide samples. Conditions of the mono-chromated Al (K) source were at 15 kV and 15 mA emission current in which the spectra of Co, Fe, ETM (i.e., V or Cr), and S 2p peaks and O and B 1s peaks were achieved at a step size of 1 eV and a pass energy of 20 eV. Field-emission scanning electron microscopy (FESEM) images were collected using an FEI/ThermoScientific ApreoS SEM through an acceleration voltage of 2 kV and equipped with ETD and in-lens Immersion detectors. For crystallographic structure at the atomic scale, an FEI Talos F200 was used to produce high-resolution transmission electron microscope (HRTEM) images. Powder XRD spectra were collected by a Rigaku Ultima IV Multipurpose X-ray Diffractometer (Rigaku Corp., Tokyo, Japan) and used for the comparison. The diffractometer was equipped with a radiation source of Cu-Ka, cross beam optics, fixed monochromator and a scintillation counter. The radiation source was emitted at 40 kV and 40 mA. A divergence slit of 2/3^{o}, divH.L. slit of 10 mm, a scattering slit of 2/3^{o}, and a receiving slit of 0.3 mm were used to collect the XRD data on a continuous scan mode in the range of 20-80^{o}. In addition, a scan speed of 1^{o}/minute and a step width of 0.02^{o} were applied. To determine the vibrational and rotational states of molecules in the samples, Raman Spectroscopy (Thermo fisher scientific DXR) was used at an excitation wavelength of 532 nm and a focused scan range of 40 – 1250 cm^{-1}. Results were attained after 40 times scan, and a laser power of 10 mW through 50-times microscope objective was used to test for the aqueous CER products in the solution (i.e., HClO in neutral pH), the N, N-diethyl-p-

phenylenediamine (DPD) method was used through the Hach kit (Hach, USA). The background concentration of free chlorine from the buffer salt impurities was subtracted from the quantified concentration of CER products after of the designated time of chronoamperometry testing. Further, the rate of CER production was quantified by dividing the CA time by the net concentration of CER products.

2.4 Electrode Preparation

Samples of the electrocatalyst powder were drop-casted on freshly polished glassy carbon electrodes (GCE; 0.072 cm^2, Gamry), for electrochemical measurements that were performed using GCE. For each sample, preparing a homogeneous slurry was done by the addition of 2 mg of the catalyst powder to 540 µL ink solution (400 µL of deionized water (DIW), 100µL of IPA, and 40 µL of Nafion). The ink was then sonicated in a 2 mL plastic vial through insertion in a water bath for a duration of 30 seconds under tip sonication. Furthermore, on the polished GCE base, 15 µL of the ink was drop-cast. The slurry was then left to dry at a temperature of 40°C for 30 minutes on top of the GCE, resulting in a catalyst loading of 0.52 mg cm^{-2}. For testing on metallic nickel foam (NF) substrate, the as-purchased NF (Latech, Singapore) was pre-treated through sonication in a mild acid bath. The optimum S,B-(CoFe(ETM)OOH@NF were drop-casted through a well-accepted method[34]. Briefly, 80 mg of the catalyst powder was dispersed in a mixture of IPA, DIW, and Nafion (6:5:0.8 vol%, 5.9 mL total volume) and the mixture was ultrasonicated for 1-hour, followed by coating of the dispersion ink on pre-treated NF substrate.

2.5 Electrochemical Characterization

An electrochemical workstation (Gamry Reference 3000) was utilized for all the electrochemical experiments. The electrochemical measurements that were carried out were

hosted by a customized 3-electrode cell. Furthermore, a standard Ag/AgCl reference electrode, a working electrode (GCE), and a counter electrode (graphite rod) were employed. Different saline pH electrolyte tests were performed on the catalysts, as such, alkaline saline (1M KOH + 0.6M NaCl), neutral saline (1M PB + 0.6M NaCl), and near neutral saline (1M $KHCO_3$ + 0.6M NaCl) were prepared to test the catalytic performance at different pH values and buffers. To avoid the accumulation of bubbles on the bare catalytic surface of the GCE, the electrolyte was stirred consistently. Moreover, to ensure the current stabilization, 10 cycles of cyclic voltammetry (CV) were undertaken from the 1-2 V (vs. RHE) potential window, followed by linear sweep voltammetry (LSV) at the same conditions. A step size of 2 mV and scan rate of 10 mV/s were utilized for CV and LSV testing. Overpotential determination involves the disregarding of the pre-oxidation peak effects on the catalytic densities; therefore, the overpotential values were reported based on LSV polarization data acquired from the positive to negative potential direction. To verify whether the potential window respective of the pH value of the electrolyte was achieved, Eq. 1 was used:

$$E\ (RHE) = E\ (Ag/AgCl) + 0.059\ pH + 0.1976 \qquad (1)$$

During any polarization experiment (i.e., CV or LSV), the value of E (RHE) occurs between 1-2 V vs. RHE. Therefore, based on Eq. 1, E (Ag/AgCl) will vary depending on the bulk pH value. Ag/AgCl was utilized as the alkaline pH 14 reference electrode whereas the standard calomel electrode (SCE) was employed for near-neutral pH experiments. When fixing the reference potential in near-neutral electrolyte experiments, the equilibrium potential of SCE used was 0.244 V (vs. RHE).

Electrochemical impedance spectroscopy (EIS) at an amplitude of 5 mV input was performed to determine the uncompensated resistances (R_s) and charge transfer resistances (R_{ct}). at a frequency ranging from 1 MHz to 1Hz. The former resistance was applied for conducting 90% IR corrections on the IR corrected polarization curves presented in this work. Linear fitting the plot of "*log(i)* vs. η" assisted in the determining of Tafel slopes. Furthermore, CV cycles were done at different scan rates (from 10 to 70 mV/s) in the pre-OER region, usually between 1.06 to 1.16 V (vs. RHE), to calculate the double-layer capacitance (C_{dl}). The C_{dl} was then obtained through the linear fit between "Δi vs. scan rate" slope, where the difference in current density is Δi.

3. RESULTS AND DISCUSSION

3.1 Characterization

Optimization of the surface ratio of Fe, B and S was done by undergoing a facile wet chemistry process atop spinel cobalt oxide (Co_3O_4) which was synthesized through a solution combustion synthesis (SCS). This was followed by additional tuning of the surface through doping with an early transition metal (ETM), namely Cr or V doping, within the amorphous oxyhydroxide shell. The morphology of the prepared samples was investigated using FESEM. At a low magnification, the obtained FESEM images in Figures 1a and 1b show a micro- "reef" like structure for the S,B-codoped samples. A prominent difference can be qualitatively seen between the Cr and V counterparts whereby the former seems to exhibit less agglomeration. Moreover, higher magnification imaging in Figures 2a and 2f show completely different morphologies. S,B-(CoFeCr)OOH seems to style clusters of facetted nanoparticles, contrary to a highly porous and seemingly fragile nanoplate-like structure in the S,B-(CoFeV)OOH catalyst. Back-scatter imaging comparing both samples in Figures 2b and 2g show much more prominent contrast for the V-doped ternary oxyhydroxide. Exposed crystalline components would have a brighter shade relative to amorphous counterparts on the same structure. Thus, the Cr-doped ternary oxyhydroxide clearly demonstrates a more obvious distribution of the advantageous amorphous S,B-codoped ternary metallic oxyhydroxide layer covering the ordered faceted CoFeCr nanoparticles. This effect of larger amorphous oxyhydroxide surface area can be well noted by comparing Figures 2c,d and 2h,i with Figures 1c and 1d), which shows the Cr-doped oxyhydroxide in the former exhibiting a much larger surface area – corresponding to the shade region of the HRTEM image. In effect, this would translate to a larger electrochemical surface

area (ECSA), as will be discussed later. Both electrocatalysts shell layer can be seen from high magnification HRTEM images in Figures 2d and 2i, whereby lack of uniform lattice fringe spacing in the oxyhydroxide shell suggests the highly amorphous region. This is remarkable given that both Cr and V-doped ternary oxyhydroxides were prepared from the same spinel Co_3O_4 fabricated through the SCS. This would seem to indicate differing favorable morphologies during Fe and ETM co-precipitation atop the crystalline cobalt oxide under room temperature wet chemical processing. Although the S,B-(CoFeV)OOH microstructure seems to attain a higher crystalline surface area and porosity, both key towards kinetically limited pH water oxidation, the better performing S,B-(CoFeCr)OOH is more structurally rigid with an apparent larger oxyhydroxide surface area, which allows for better sustenance during high current density operation. Clear agglomeration of the S,B-(CoFeV)OOH may well be exacerbated during OER operation, due to the as-prepared interconnected structure, which would lower the available surface area for reaction further. The degree of agglomeration can also be attributed to the ETM salts utilized. High magnification HRTEM images in Figure 2d, corresponding to the S,B-(CoFeCr)OOH catalyst shows d spacings of 0.25, 0.46, 0.15, and 0.21 nm which correspond to (311) and (111) facets of Co_3O_4, spinel $CoCr_2O_4$, and Co_2B, respectively, for the Cr-doped oxyhydroxide. It shall be noted that since the presented high magnification HRTEM images are taken at the interface between crystalline Co_3O_4 and the oxyhydroxide shell, the latter's high amorphicity makes it challenging to visualize lattice fringe spacings throughout. Both S,B-(CoFeCr)OOH and its V-doped counterpart in Figure 2i show clear homogeneity of both (100) and (110) facets of Co and Fe oxyhydroxides, respectively, corresponding to a d spacing of approximately 0.24 nm. Higher electronegativities of Co and Fe, relative to the ETMs examined, allows (CoFe)OOH oxyhydroxide to still act as active sites, with enhanced electronic modulation

towards OER from the high oxidation state ETMs. Both materials have respective homogenous morphologies and elemental distributions (Figure 2e and 2j), whereby the latter is key towards ensuring no phase separation phenomenon occurring during co-precipitation. Moreover, in designing the S,B-codoped ternary oxyhydroxides, CER suppression was one of the important aspects targeted through ensuring electrostatic repulsion ability towards Cl^-. To this end, and as will be discussed later, it is pivotal to establish homogenous presence of anionic S and B throughout the oxyhydroxide. Further, EDS analyses presented in Figures 1e and 1f confirm as-desired atomic percentage distribution for the as-prepared S,B-codoped catalysts. Importantly, this demonstrates that the scalability of the synthesis method does not precede efficacy of the resultant catalyst.

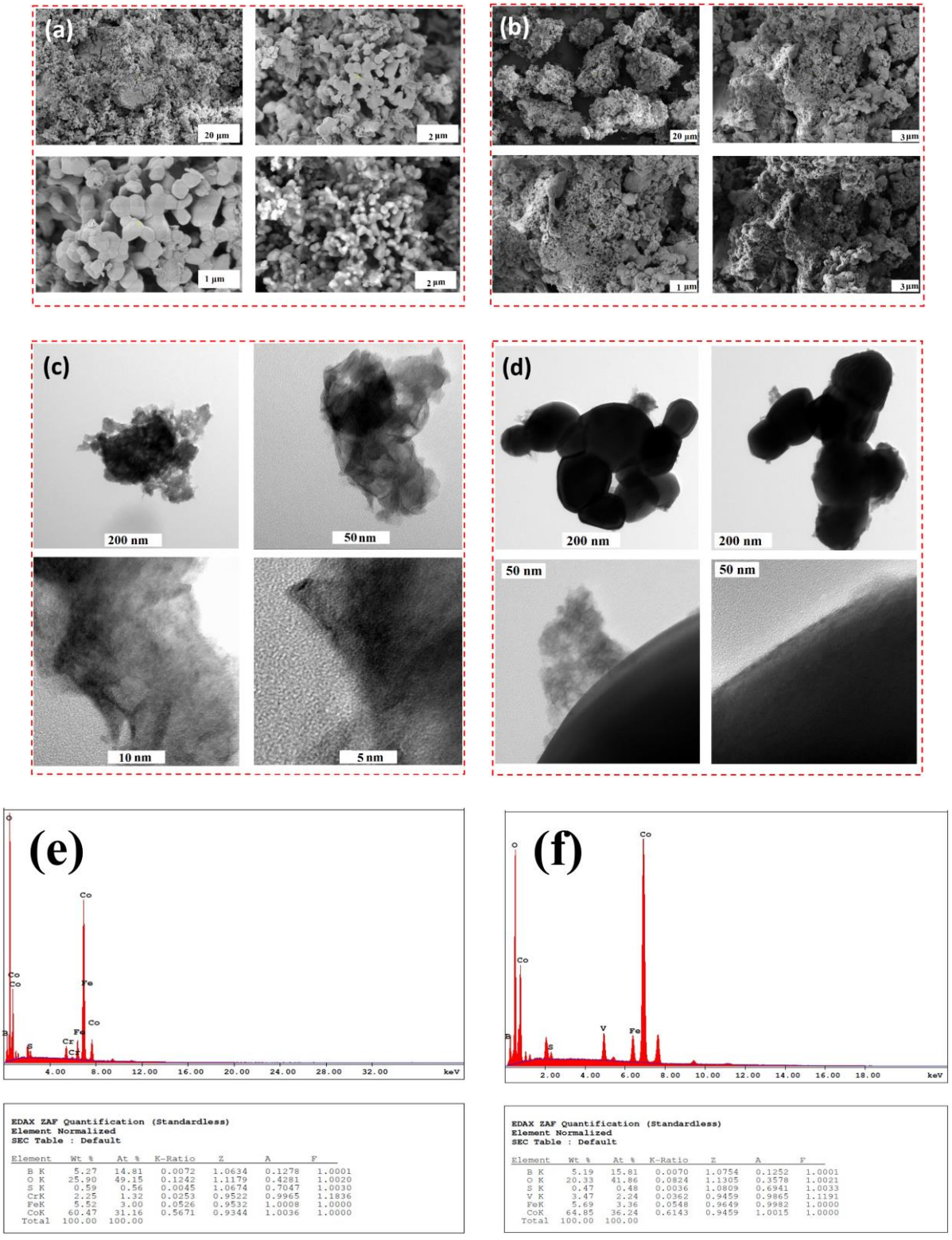

Figure 1. *FESEM and HRTEM images of (a, c) S,B-(CoFeCr)OOH and (b, d) S,B-(CoFeV)OOH under different magnifications, respectively. EDS spectra for (e) S,B-(CoFeCr)OOH and (f) S,B-(CoFeV)OOH.*

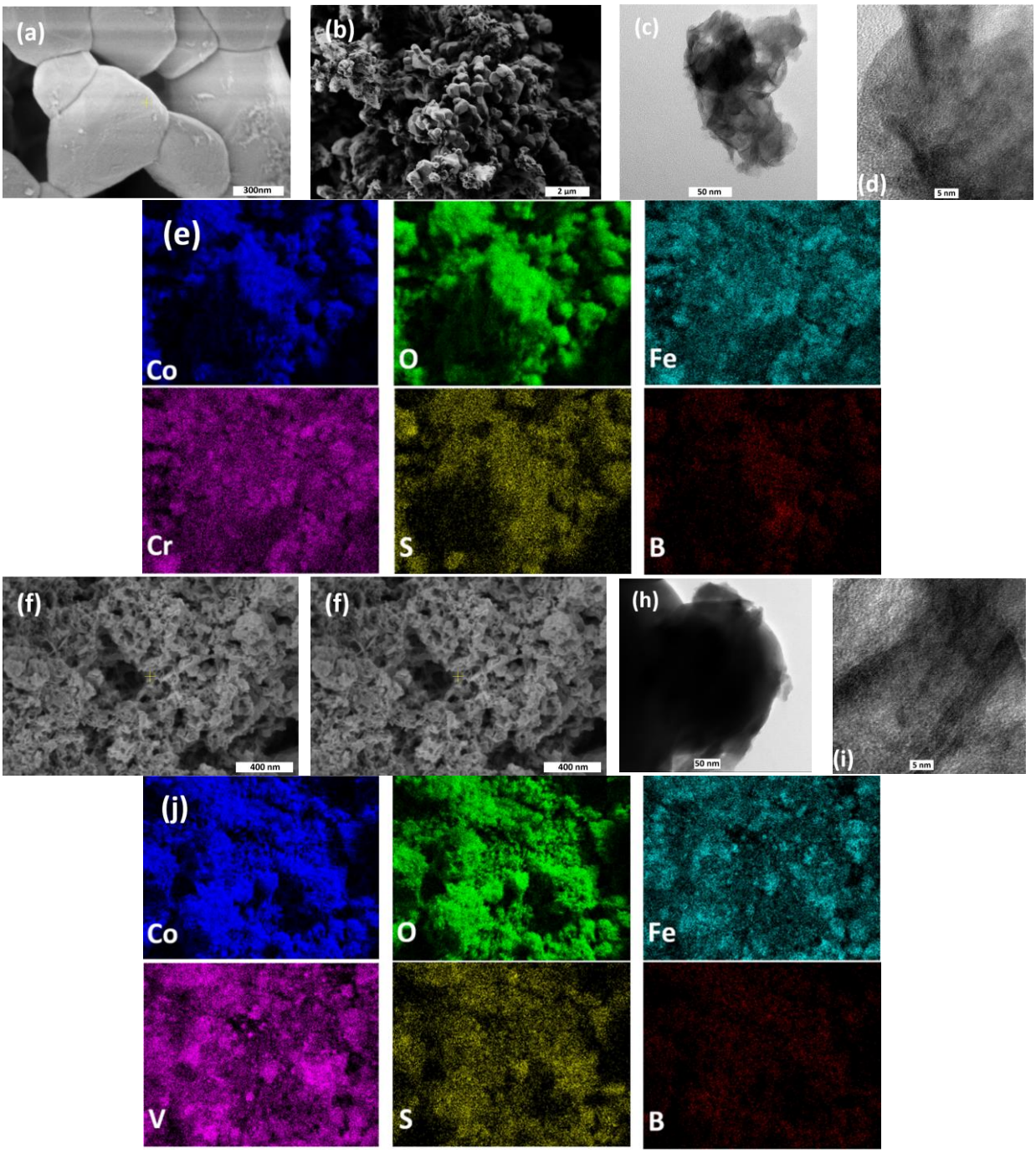

Figure 2. *(a) FESEM, (b) ETD back-scattering, (c, d) HRTEM, and (e) ESEM elemental mapping of S,B-(CoFeCr)OOH. (f) FESEM, (g) ETD back-scattering, (h, i) HRTEM, and (j) ESEM elemental mapping of S,B-(CoFeCr)OOH.*

X-ray diffraction (XRD) measurements were conducted to find the crystal structure and phase of the final product. As it can be seen from Figure 3a below the notable (311) diffraction plan that is at 36.8° represents the spinel Co_3O_4 that is present in the S,B-codoped ternary oxyhydroxides. Moreover, there are more diffraction planes at (111), (220), (222), (400), (422), (511), and (440) which correspond to peak angles of 19.0 , 31.2, 38.5, 44.8 , 55.6, 59.3, and 65.2 2θ (°) that represent the maintained spinel cobalt oxide and thus reassures the purity of the prepared oxyhydroxides[35]. However, metallic iron and early transition metal dopants are fixed in the amorphous condition and do not crystallize, which is shown by the absence of new peaks. In addition, in Figure 3a it can be seen that there are evident structural distortion through decrease of peak intensities and increase in the full-width half maximum (FWHM) of prominent peaks and this can also be seen in the (311) plane[36]. This is a result of doping the templating Co_3O_4 core. In addition, it can be seen that there is a blueshift towards higher 2θ this corresponds to Bragg's law that indicates lattice compressions in the crystals facet. Further, this is thought to be an outcome of the crystalline core and differences in ionic radii between Cr and V, Fe to ETM dopant ratios, and oxidation state distribution of cationic metallic species atop the oxyhydroxide interface interactions. Compressive strains can favorably modulate the adsorption energies of reaction intermediates towards more thermodynamically facile values as recently reported by Dionigi et al. and others that appropriate compressive strains can favorably modulate the adsorption energies of reaction intermediates towards more thermodynamically facile values [37, 38]. Moreover, in Figure 3b, Raman spectroscopy was performed on S-doped and S,B-codoped CoFeCr and CoFeV oxyhydroxides. The three main peaks indicate E_g, E_{2g}, and A_{1g} vibrational modes of basal spinel Co_3O_4 that are established in all tested samples, albeit blue shifted from accepted values of vibrational modes[39]. In addition, there is an extra blueshift in the A_{1g} mode S-

doped oxyhydroxides indicating lattice relaxations. However, indication of lattice compression can be seen in the redshifts between the S- to S,B-codoped ternary oxyhydroxides through XRD which is a result of boronation[40]. Furthermore, the ultra-fast crystallization processes during the SCS in synthesizing core cobalt oxide may well contribute towards as formed lattice distortion phenomena[41]. Moreover, on the highlighted regions there was peak broadening and obvious peak intensity decrease, relative to the pristine Co_3O_4 spectra as Lorentzian fit was performed. This may represents the degree of amorphization atop the surface[42], whereby it can be seen that S,B-codoped samples have lower peak intensities and broader peaks relative to their S-doped counterpart. As a result, S,B-codoped oxyhydroxides lead to a larger amorphic oxyhydroxide shell which reciprocates to a larger electrochemical surface area. The current density increase rate and the onset potential can be both used to measure the electrochemical actvity[43]. The current density increase rate versus the applied potential, particularly at large current densities is mainly due to the diffusion-limited schemes which is shown by the Butler-Volmer relationship. Furthermore, during OER for the diffusion-controlled the limiting current (i_{lim}) can be described as follows:

$$i_{lim} = C^* \frac{zFD}{\delta} \qquad (3)$$

*C** here presents the bulk concentration of electroactive species, *D is* the diffusion coefficient *z* is the number of electrons involved in the reaction, δ is the diffusion layer thickness, and *F* is the Faraday's constant. Therefore, from the equation it can be directly see that i_{lim} and δ are inversely proportional which is a result that can be capitalized on through catalyst design. Furthermore, hydrophilicity and aerophilicty have an inverse relationship. Hydrophilicity factor is an essential component specifically when dealing with designing water oxidation catalysts in order to perform well in neutral and near-neutral pH environments[44]. Moreover, under these conditions

H_2O absorption to the surface becomes the intial step in the OER mechanism. Therefore, improving the surface hydrophilicity that is thought to turn complement advantageous kinetics in neutral pH water oxidation.

Moreover, the reasoning behind anionic co-doping with S and B was to target improved hydrophilicities. This can be seen when the following contact angle measurements were compared which are S,B-codoped and S-doped ternary oxyhydroxides in Figure 3c, d and Figure 3e, f, respectively. A significant affinity towards surface water absorption is attained. S-(CoFeCr)OOH showed a high contact angle of 121.9º, which was then extensively decreased to 56.8º as additional boronation was done. Thus, a symbiotically favorable aerophobic and hydrophilic surface would see towards fast O_2 bubble rejection from the catalytic surface upon formation at high current density operations, thinning the bubble/gaseous layer atop the catalyst[45]. Therefore, this leads to an increase in the OER diffusion intermediates and a decrease in δ. Hydrophilic affinity of the surface enhances its diffusion further when H_2O is the main intermediate for OER in near-neutral pH media. In effect, this leads to curbing kinetic hinderances during near-neutral pH OER.

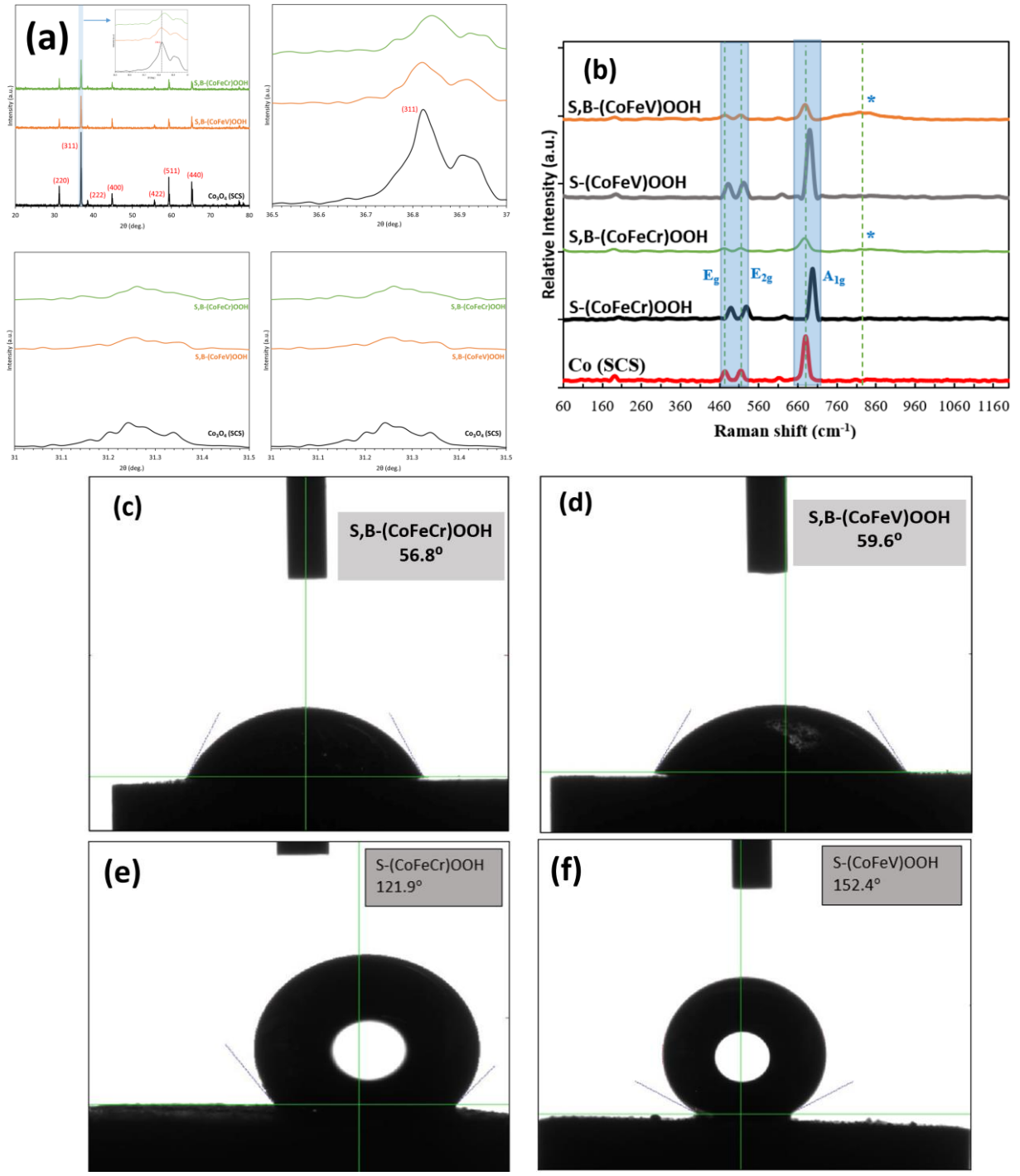

Figure 3. *(a) XRD patterns of as prepared spinel Co_3O_4 (SCS) and the S,B-codoped (CoFe(ETM))OOH oxyhydroxides. Inset shows blueshift of prominent (311) phase in S,B-(CoFeCr)OOH relative to core Co_3O_4 at different diffraction ranges, and (b) Raman spectra of Co_3O_4 (SCS), S-doped, and S,B-codoped ternary oxyhydroxide. Contact angle measurements atop drop-casted (c) S,B-(CoFeCr)OOH, (d) S,B-(CoFeV)OOH, (e) S-(CoFeCr)OOH, and (f) S-(CoFeV)OOH.*

X-ray photoemission spectroscopy (XPS) technique was done in order find the chemical states of surface elements in the S-doped and S,B-codoped ternary oxyhydroxides to ensure effective doping was successful, and suggest surface oxidation changes that may occur after OER electro-activation. In addition, in figure 4a in the O 1s core-level spectra it can be seen that there are three different binding modes which are defective or low coordination oxygen from M-OOH, lattice oxygen, and hydroxyl groups from adsorbed surface H_2O[46, 47]. In addition, the latter peak is particularly in larger ratio of the Cr-doped relative to the V-doped oxyhydroxide. This is an indirectly implies a favorable hydrophilicity of the former. This is a result of the several oxygen containing species, such as SO_3^{2-}/SO_4^{2-}/BO_3^{3-} whom have an overlap in high binding energies with adsorbed H_2O. Also, the last peak in both samples might represent a mixture of few chemisorbed oxygen containing species. Furthermore, it can be seen that there are splitting into $2p_{3/2}$ and $2p_{1/2}$ due to spin-orbit coupling that happens in the cationic metallic components, i.e., Co (2p), Fe (2p), Cr (2p), and V (2p) when they underwent detailed analysis. Spin-orbit coupling of Co $2p_{3/2}$ and $2p_{1/2}$ at 781.6 and 797.4 eV can be seen in Figure 4b for the S,B-codoped oxyhydroxides. In addition, there were three smaller peaks at binding energies of 781.8, 783.5, and 789.5 eV corresponding to Co^{3+}, Co^{2+}, and a satellite peak, due to the peak deconvolution of the $2p_{3/2}$ split[48].

Furthermore, there can be seen an energy difference between 2p spin-orbits which was 0.8 eV and larger than that of pristine spinel Co_3O_4 (15 eV)[49], this can as a result to the presence of Co^{3+} character in the as prepared catalysts. Further, in Figure 4c there can be seen Fe 2p deconvolution which represents dominant $2p_{3/2}$ peaks complimenting Fe^{2+} and Fe^{3+} states which are interestingly blue-shifted by about 1.35 eV in the S,B-(CoFeCr)OOH spectra. These shifts imply a strong electron correlations between Co and dopant Fe and Cr[50]. Moreover, to regulate

the oxidation state of electroactive Co sites through the so-called 'regulating effect'[6] early transition metals were doped on the oxyhydroxides. The main idea behind this theory is to maintains Co active sites at lower oxidation states, namely Co^{2+}. This is done in order to enhance the formation of oxygen vacancies during which were shown to improve the performance of the catalyst and to limit the rate-determining Co^{3+}/Co^{4+} transition during OER operation[51]. Also, it can be clearly seen in Figure 4d for the early transition metals 2p spectra for S,B-(CoFeV)OOH, that vanadium is at a binding energy of 514.3 eV which represents V^{3+} state[13]. However, on the other side the S,B-(CoFeCr)OOH resulted in Cr^{2+} and Cr^{5+} states at binding energies of 574.82 and 577.29 eV, respectively, for the Cr $2p_{3/2}$ spin-orbit[52]. Continuing on with anionic dopants, in Figure 4e for the S 2p fitting it can be seen that there is a small M-S bonds in the $2p_{3/2}$ spin-orbit region at a binding energy of 161.8 eV for the Cr-doped oxyhydroxide. This is well known to regulate the electronic structure of the surface towards OER[53,54]. Moreover, low coordination $2p_{1/2}$ spin-orbit peaks at 166 and 167.4 represent SO_3^{2-} and SO_4^2. Those are known to improve the hydrophilicity and this was proofed through the contact angle measurements for both S,B-codoped oxyhydroxide[55, 56]. In addition, in Figure 4f the B 1s shows a dominant peak that represents the oxidized boron species which also improves hydrophilicity[17]. The spectra in Figure 4g prove the existence of Co, Fe, ETM (Cr or V), S and B (for boronated samples). Furthermore, anionic S and B species atop the oxyhydroxide provided a well dispersed electronegativity cloud which can protect active metallic oxyhydroxide sites from incoming chloride ions in saline water electrolytes, in effect curbing the CER kinetics under such conditions.

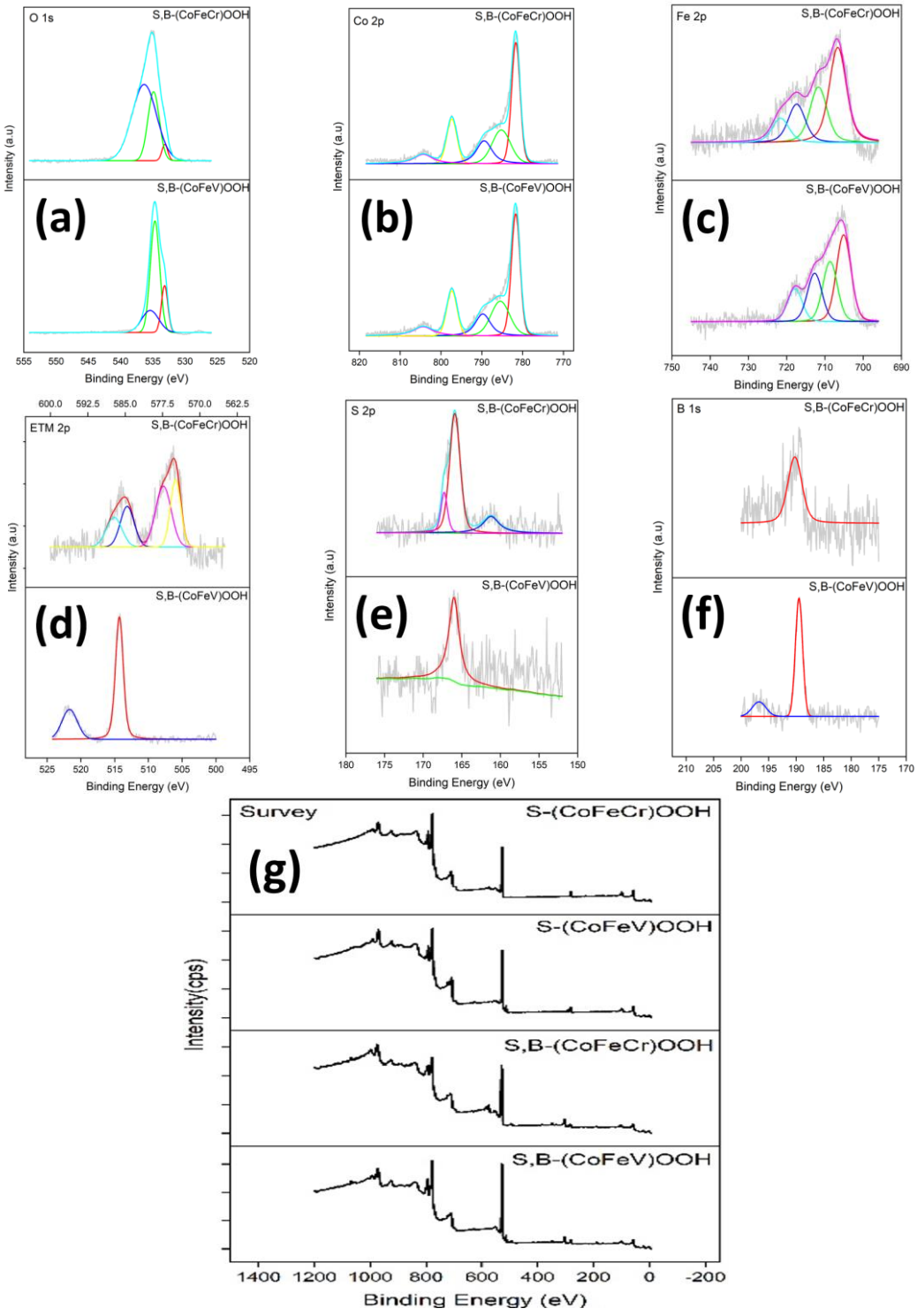

Figure 4. *Peak fitted high resolution XPS spectra of (a) O 1s, (b) Co 2p, (c) Fe 2p, (d) ETM 2p, (e) S 2p, and (f) B 21s for the as prepared S,B-(CoFeCr)OOH and S,B-(CoFeV)OOH samples. (g) XPS full survey of S and S,B-codoped ternary oxyhydroxide electrocatalysts.*

3.2 Alkaline Saline Water Oxidation

In addition to the main aspects studied in this research, a side-aspect was investigated which is the water oxidation screening at high pH values. This is important for the catalysts' performance comparison purposes, especially in terms of overpotential and Tafel slopes. Additionally, performing this investigation provides better explanations for the improved performance of the catalysts, considering that the focus of the literature reviews and the current top-research studies is limited to alkaline water oxidation (1M KOH). Therefore, in order to investigate the performance of the as-prepared oxyhydroxide catalysts, several media were tested. The first test was run in a saline alkaline (1M KOH + 0.6M NaCl) electrolyte, with a pH value of 14. The results are shown in Figure 5a, which represents the polarization curves of the two S- and two S,B-codoped ternary oxyhydroxide catalysts in the said electrolyte. From the data obtained, it was found that in order to achieve a current density of 10 mA cm^{-2}, the S-doped samples – i.e. S-(CoFeCr)OOH and S-(CoFeV)OOH – required low overpotential values of 232 and 235 mV respectively. When the same catalysts were boronated – i.e. S,B-(CoFeCr)OOH and S,B-(CoFeV)OOH, it was found that in order to achieve the same current density of 10 mA cm^{-2}, the samples required overpotential values of 198 and 218 mV respectively. However, in order for these catalysts to be used in real-life applications, the catalyst need to achieve higher current density values, such as values above 500 mA cm^{-2} for extended periods of time. According to Figure 5a with 90% *iR* corrected polarization curves, the current density of 500 mA cm^{-2} by overpotential values of 426, 428, 322, and 388 mV for S-(CoFeCr)OOH, S-(CoFeV)OOH, S,B-(CoFeCr)OOH, and S,B-(CoFeV)OOH, respectively. When it comes to the competing and undesired chlorine evolution anodic reaction (CER), the alkaline design criteria present thermodynamic limitations to the CER in the pH range of 7.5 to 14, requiring less than 480 mV

regardless of the current density value[30]. As a result, it can be expected that all of the catalysts investigated in this research, namely S-(CoFeCr)OOH, S-(CoFeV)OOH, S,B-(CoFeCr)OOH, and S,B-(CoFeV)OOH, should have 100% selectivity towards the OER rather than the CER when operating at 500 mA cm-^{2}, as the overpotentials needed to achieve that current density are below 480 mV. Figure 5b represents that Tafel slopes of the two S- and two S,B-codoped ternary oxyhydroxide catalysts in the same electrolyte. From the polarization curves presented, generally it can be seen that the OER kinetics are enhanced as the catalysts are boronated (i.e. going from S to S,B-codoped catalysts). This is supported by the lowered Tafel slope values for each pair of S-doped and S,B-codoped catalysts. Furthermore, the S,B-(CoFeCr)OOH catalyst had the superior kinetics of all , which is indicated by the lowest value of 45.3 mV/dec. In order to test the S,B-codoped catalysts' stabilities in the same electrolyte environment, 1000 cycles of cyclic voltammetry (CV) were run, and subsequently the LSV polarization curve was recorded to detect if there are any changes in the current response, as conveyed in Figure 5c.

After 1000 CV cycles, the current response of S,B-(CoFeV)OOH catalyst uniformly decreased by 150 mA cm^{-2} approximately at a specific limiting potential. The lowered performance may be the result of the chloride corrosion, which can form inert metal chloride surface sites, hence deactivating some of the electrochemical surface area[31]. On the other hand, the current response of S,B-(CoFeCr)OOH decreased by 50 mA cm^{-2} approximately at lower potentials until 1.56 V (vs. RHE), after which the current response increases (i.e. becomes stronger) far more than the initial LSV curve. A possible reason for this performance is the improved kinetics achieved as a result of the additional electro-activation, which can be especially shown at higher current densities that are known for being diffusion-limited.

Moreover, the superior performance of S,B-(CoFeCr)OOH catalyst over its V-based counterpart can be also attributed to the electrochemically active surface area (ECSA), which was calculated using double-layer capacitance (C_{dl}) as shown Figure 5d. From the calculations, it was found that around 660 cm^2 ECSA is acquired for the co-doped Cr-based catalyst, which is approximately 20% greater than that of the S,B-doped V-based sample. This is further supported by the difference in the HRTEM images in Figures 1c and 1h. Additionally, as witnessed in figure 5d, the ECSA increases upon boronation for both the co-doped Cr and V-based catalysts. Therefore, it can be confirmed that the increased ECSA enhances the performance of the superior catalyst. Furthermore, the charge transfer resistance (R_{CT}) was studied through the EIS Nyquist plots shown in Figure 5e. The S,B-codoped oxyhydroxides presented advantageously lowered R_{CT} values compared to the S-doped oxyhydroxides, which supports the superiority of the S,B-codoping strategy by presenting its key intrinsic enhancements. Among the various reasons, the variations in the surface chemistry of the co-doped catalysts is one possible reason for the increased conductivity. To elaborate on that, the oxygen defects are greater in the co-doped catalysts than in the S-doped catalysts, and that increase is accompanied by a decrease in the energetic separation between the band centers of oxygen 2p and metal 3d, according to density functional theory (DFT) studies in similar electrocatalytic systems[51]. Consequently, the conductivity increases and the surface's electronic structure is modulated, resulting in an improved electron transfer rate in the sluggish $4e^-$ OER process.

Thus, to summarize, it can be inferred and confirmed that the best-performing and most stable catalyst out of the two S- and two S,B-codoped ternary oxyhydroxides in alkaline saline condition is the S,B-(CoFeCr)OOH catalyst, as proved by the low overpotential value at high current density, stability after 1000 CV cycles, increased conductivity, ECSA, and Co^{2+}/Co^{3+}

transition (Figure 3b) during OER. Figure 5f presents the Tafel slopes and overpotential values at a current density of 10 mA cm^{-2} for some of the most promising and newly reported OER catalysts in alkaline water environment (1M KOH). Compared to these data, it can be seen that S,B-codoped oxyhydroxides rank amongst the kinetically favorable Tafel slopes with some of the lowest reported overpotentials to date.

Further, the two S,B-codoped oxyhydroxides were deposited on metallic nickel foam (NF). This was done in order to promote lower charge transfer resistances, and improve the kinetics by the increased porosity of the substrate, in addition to a number of other benefits stated earlier. In order to achieve a current density of 10 mA cm^{-2}, S,B-(CoFeCr)OOH@NF and S,B-(CoFeV)OOH@NF required overpotential values of 164 and 176 mV respectively, which are 34 and 43 mV lower than without NF deposition. Likewise, the Tafel slopes of S,B-(CoFeCr)OOH@NF and S,B-(CoFeV)OOH@NF decreased to 34.2 and 38.4 mV/dec. Remarkably, these NF-deposited oxyhydroxides outperform the commercial benchmark IrO_2@NF catalysts, which required 365 mV overpotential to achieve a current density of 10 mA cm^{-2}, and presented a Tafel slope of 55 mV/dec[57].

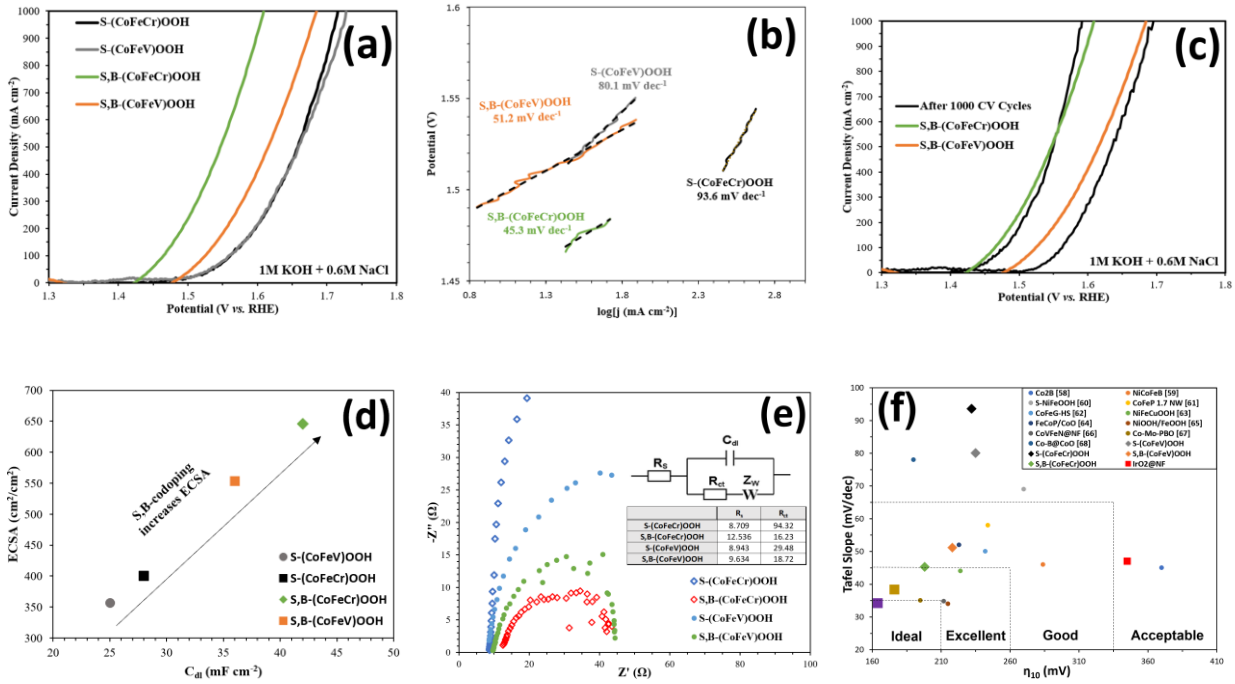

Figure 5. *(a) Polarization curves, (b) Tafel slopes, and (c) LSV curves before and after 1000 cycles of CV for the two S- and two S,B-codoped ternary oxyhydroxide catalysts in alkaline saline electrolyte (1M KOH + 0.6M NaCl; pH=14). (d) Electrochemically active surface area (ECSA) versus double layer capacitance (C_{dl}) and (e) Electrochemical impedance spectroscopy (EIS) Nyquist plots of as prepared ternary oxyhydroxides. The inset table records the attained solution uncompensated resistances (R_s) used for 90% iR corrections of all polarization curves and charge transfer resistances (R_{CT}) in alkaline saline electrolyte. (f) Comparison of Tafel slopes (mV/dec) versus overpotentials (mV) at current density equaling 10 mA cm^{-2} for recently reported high performing OER electrocatalysts in alkaline water (1M KOH) electrolyte* [58-68]*. This work's data presented in the same figure are attained from alkaline saline water oxidation.*

Based on the high performing polarization results attained by the S,B-(CoFe(ETM))OOH materials and the corresponding low Tafel slopes, we seek to investigate the OER mechanism at play. Conventionally, the adsorbate escape mechanism (AEM) propagates through several OER adsorbed intermediates (i.e., OH*, O*, and OOH*, where asterisk (*) signifies an active site) until finally transforming to O_2[69]. Cobalt oxyhydroxide (i.e., CoOOH) and traditional benchmark IrO_2 and RuO_2 electrocatalysts for OER predominantly progress through the AEM under which a minimum theoretical overpotential required is to be greater than 370 mV. The attained

overpotentials of the developed S,B-codoped ternary oxyhydroxides breaks this conventional mechanism's limitations and achieved higher performance through lower overpotentials. This turns focus towards the lattice oxygen migration (LOM) mechanism, which bypasses the aforementioned overpotential limitation[70]. LOM typically implicates lattice oxygen transformation through O-O coupling into OER intermediates whilst replenishment of the site with hydroxyls in the electrolyte[71]. This effect can entail lattice oxygen transforming to oxyhydroxides upon OER electro-activation, as confirmed from post-OER O 1s peaks of S,B-(CoFeCr)OOH in Figure 6a. Thus, the S,B-codoping strategy not only facilitates for a larger amorphous ECSA, but also allows for a shift in the OER mechanism where $M–O_x(OH)_y$ (i.e., M is Co, Fe, ETM) are the catalytic species for OER under the LOM.

Furthermore, in order to investigate chemical state changes, stability, and further offer explanation towards attained performance, post-OER surface chemistry characterization through XPS was undertaken. Figure 6a shows that upon electro-activation, no presence of lattice oxygen is witnessed in the S,B-(CoFeCr)OOH oxyhydroxide. Instead, predominant oxygen content transforms towards higher binding energies representing M-OOH in formulating the oxyhydroxide structure. A similar phenomenon is seen for the S,B-(CoFeV)OOH sample, although to a lesser extent. This may explain the variability in ECSA attained from C_{dl} data and accounts for how oxyhydroxide layer is thickened upon electro-activation. Furthermore, Co $2p_{3/2}$ spin-orbits in Figure 6b shows that Co^{2+} content advantageously increases in S,B-(CoFeCr)OOH relative to the pre-OER peaks in Figure 4b. Contrarily, the opposite effect is seen to happen for the S,B-(CoFeV)OOH which sheds light on why the Cr-doped oxyhydroxide attained lower overpotentials for the same current densities. The ratio of Fe^{3+}/Fe^{2+} in both materials increases after OER electro-activation, as seen in Figure 6c, suggesting a symbiotic redox relationship

between Co and Fe, as initially indicated through blueshifts in the pre-OER Fe 2p peaks. Further, Figure 6c shows that both ETMs are shifted towards higher binding energies upon OER, whereby a shift from V^{3+} to V^{5+} and from Cr^{2+} to Cr^{6+} is evident for S,B-(CoFeV) and S,B-(CoFeCr), respectively. This confirms the regulating effect intended by ETM doping through which electrons generated through formation of higher oxidation state ETMs reduce and maintain electro-active CoOOH in a preferentially low oxidation state of Co^{2+}. This corresponds to β-CoOOH which is the most active site rather than higher valence Co in γ-CoOOH[6]. Interestingly, upon electro-activation in alkaline environments, the oxidized sulfur character is majorly shifted towards lower binding energies at 162.6 eV corresponding to M-S bonds[54], which are known to optimize surface electronics towards favorable OER in alkaline conditions, as can be seen in Figure 6e. Lastly, upon alkaline OER operation, the B 1s spectra for S,B-(CoFeCr)OOH in Figure 6f shows an increase in oxy-boride character relative to elemental boron, which is the opposite effect observed for the S,B-(CoFeV)OOH. In fact, a high degree of boron leaching is evident in the S,B-codoped V-based oxyhydroxide. Slight bulges in the raw spectra for B 1s at higher binding energies are believed to correspond to chloride character from the alkaline saline water medium used for electro-activation. It would be interesting to investigate how the oxidized S and B character changes upon OER in neutral pH conditions. However, we believe that under neutral pH environments, $SO_x^{\delta-}$ and $B_yO_x^{\delta-}$ anionic content to be maintained considering that hydrophilicity is well maintained.

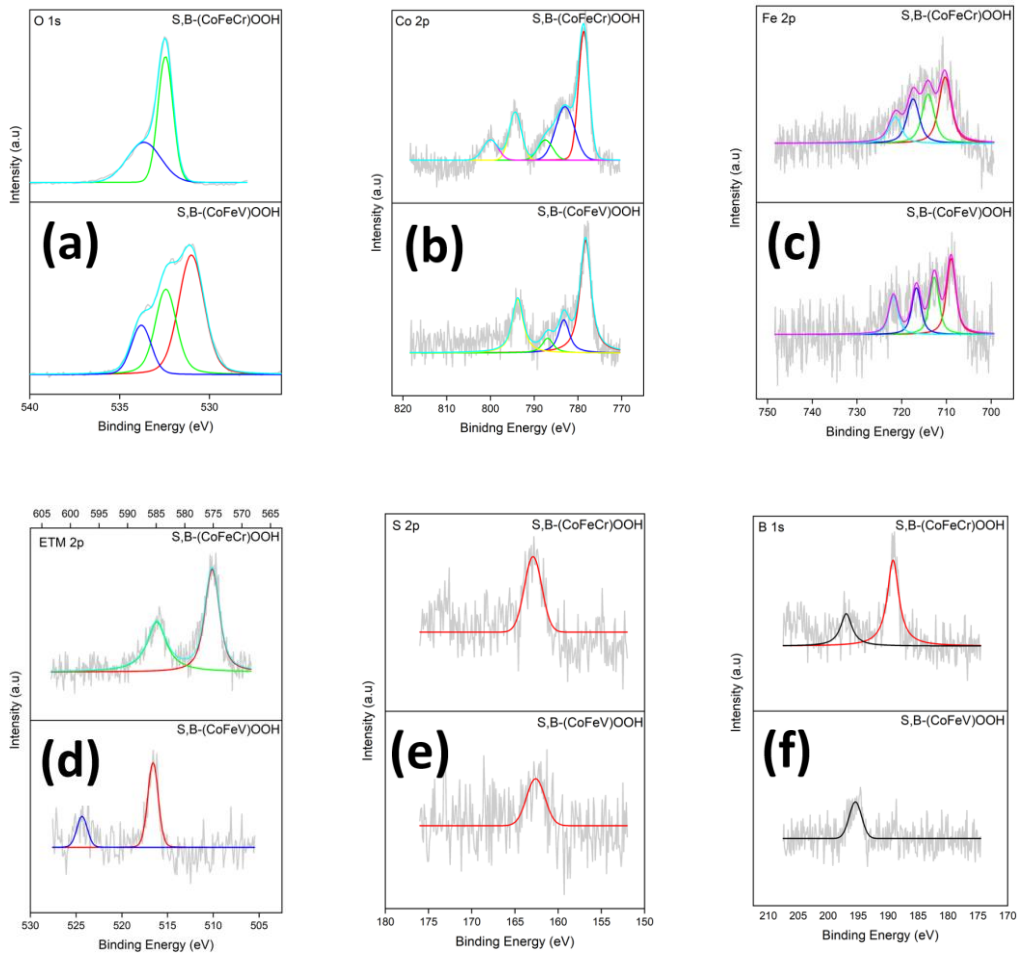

Figure 6. *Peak fitted high resolution XPS spectra of (a) O 1s, (b) Co 2p, (c) Fe 2p, (d) ETM 2p, (e) S 2p, and (f) B 21s for S,B-(CoFeCr)OOH and S,B-(CoFeV)OOH samples after OER testing.*

3.3 Near-neutral Saline Water Oxidation

Of practical interest towards industrial realization of seawater electrolysis, the performance of the S,B-codoped ternary oxyhydroxides was investigated in near-neutral pH saline conditions. Figure 7a displays the attained LSV polarization data for both S,B-codoped ternary oxyhydroxides in near-neutral pH bicarbonate-buffered saline (1M $KHCO_3$ + 0.6M NaCl; pH ~ 8 ±0.1) and neutral phosphate-buffered saline (1M PB + 0.6M NaCl; pH ~ 7 ±0.1)

electrolytes. Both S,B-(CoFeCr)OOH and S,B-(CoFeV)OOH oxyhydroxides performed well whereby overpotentials of 353 and 408 mV, respectively, were required to achieve a current density of 100 mA cm^{-2} in saline bicarbonate electrolyte. Moreover, higher overpotentials of 505 and 546 mV were required to reach the same current density in neutral saline electrolyte for the Cr and V-doped catalysts, respectively. Both these results compare very well with contemporary near-neutral and neutral pH water oxidation anodes recently reported[22, 72]. The promising performances of the developed oxyhydroxides in near-neutral pH conditions is believed to be strongly correlated to the high degree of hydrophilicity of the developed S,B-codoped oxyhydroxides. Since water molecules are the initial OER intermediate in near-neutral pH conditions, it is extremely important to have appropriate surface energetics for facile water adsorption; and high hydrophilicity is indicative of a strong water binding energy. In interest towards ensured prolonged stability in neutral pH saline environments, both catalysts were tested for 50 hours chronoamperometrically at a fixed current density of 50 mA cm^{-2}, as displayed in Figure 7b. Although both oxyhydroxides endure some performance loss after some hours, the S,B-(CoFeCr)OOH required an additional 17 mV of overpotential at the end of the 50 hours to maintain the same current density, which is considerably better than stabilities previously reported in similar conditions[73, 74]. Further, it shall be noted that part of the increase in required potential may be due to minor chipping of electrocatalyst powder from the GCE tip due to bubble formation.

To address this potential issue, we deposited the two optimum S,B-codoped ternary oxyhydroxides on NF to lower risk of mechanical etching due to bubble formation at high current densities and to offer a substrate that is more porous to ameliorate kinetic limitations intrinsic to neutral pH electrolysis. Figure 7c shows the attained chronopotentiometric (CP)

stability testing of both S,B-(CoFeCr)OOH@NF and S,B-(CoFeV)OOH@NF in neutral saline electrolyte; Figure 7d displayed the full 50-hours of testing. As can be seen, the attained current density increases almost 4 times when the ternary oxyhydroxides are deposited on pre-treated NF. This enhancement in performance is witnessed more pronouncedly for the Cr-based oxyhydroxide, suggesting that registered performance of the oxyhydroxide on GCE is severely kinetically hindered. Moreover, for both S,B-codoped catalysts on NF, stability is very well ensured at an applied potential of 1.71 V (vs. RHE). Since CP operation was conducted in neutral pH saline environment, the thermodynamic potential required for CER to occur is calculated to be 1.70 V (vs. RHE). Thus, operating at 10 mV over the required limiting potential for CER allows examination of CER suppression effects of the different oxyhydroxides. Furthermore, it shall be noted that significant local pH drops near the anode surface are expected when operating at high current densities in bulk neutral pH systems, further decreasing the thermodynamic limit requirement for CER[75, 76]. The DPD method was used to quantify evolved chloro-reaction products (i.e., HClO)[77]. Insets in Figure 7c show liquid vials with pink solution after adding the DPD agent to the electrolyte solution after CP experiments and a higher intensity of the color indicates a higher concentration of CER products. HClO formation was calculated as a rate for a more representative averaging of generated CER products per unit time. Consequently, a lower rate of CER would indicate more selective OER and thus more suppressed CER. S,B-(CoFeCr)OOH and S,B-(CoFeV)OOH deposited on GCE were operated at 1.71 V (vs. RHE) for 6 hours and attained CER products generation rates of 0.108 and 0.148 mg per liter per hour (mg $(Lh)^{-1}$). Clearly the Cr-doped counterpart offered a higher affinity towards OER and it is expected to be a result of two main interconnected phenomena. Firstly, the stronger electrophilic property of higher valence state of Cr^{6+} upon electro-activation results in a

higher electron localization effect on bound oxyhydroxide group ($Cr^{\delta+}(OOH)^{\delta-}$) which activates stronger electrostatic shielding from anionic Cl^- without significantly affecting flux of incoming feed H_2O molecules for OER. Secondly, the larger oxyhydroxide layer confirmed earlier in Figures 1c and 4d allows for a more thorough shielding area from incoming Cl^- ions. Furthermore, we have tested the same oxyhydroxides deposited on NF under the same electrolytic and potentio-static conditions, but for 50 hours. This was performed after obtaining polarization curves in neutral saline electrolyte, presented in Figure 7e. We find that the generation rate of CER products decreases significantly for both the Cr and V S,B-codoped analogues corresponding to 0.014 and 0.044 mg $(Lh)^{-1}$ of total chlorine. This either indicates an effect that the NF substrate plays towards suppressing CER, which seems unlikely from a chemical standpoint, or implies that CER may be occurring in the first few hours of operation then slows down upon catalyst surface reconstruction. This finding warrants a dedicated study on the effect. Unfortunately, within the small saline/seawater electrolysis research community a yet smaller number of groups report testing in neutral pH conditions. Although an exponentially growing field, there were no quantifiable CER production rates we could compare with. Nevertheless, it is our firm motivation that this work would offer a stepping stone.

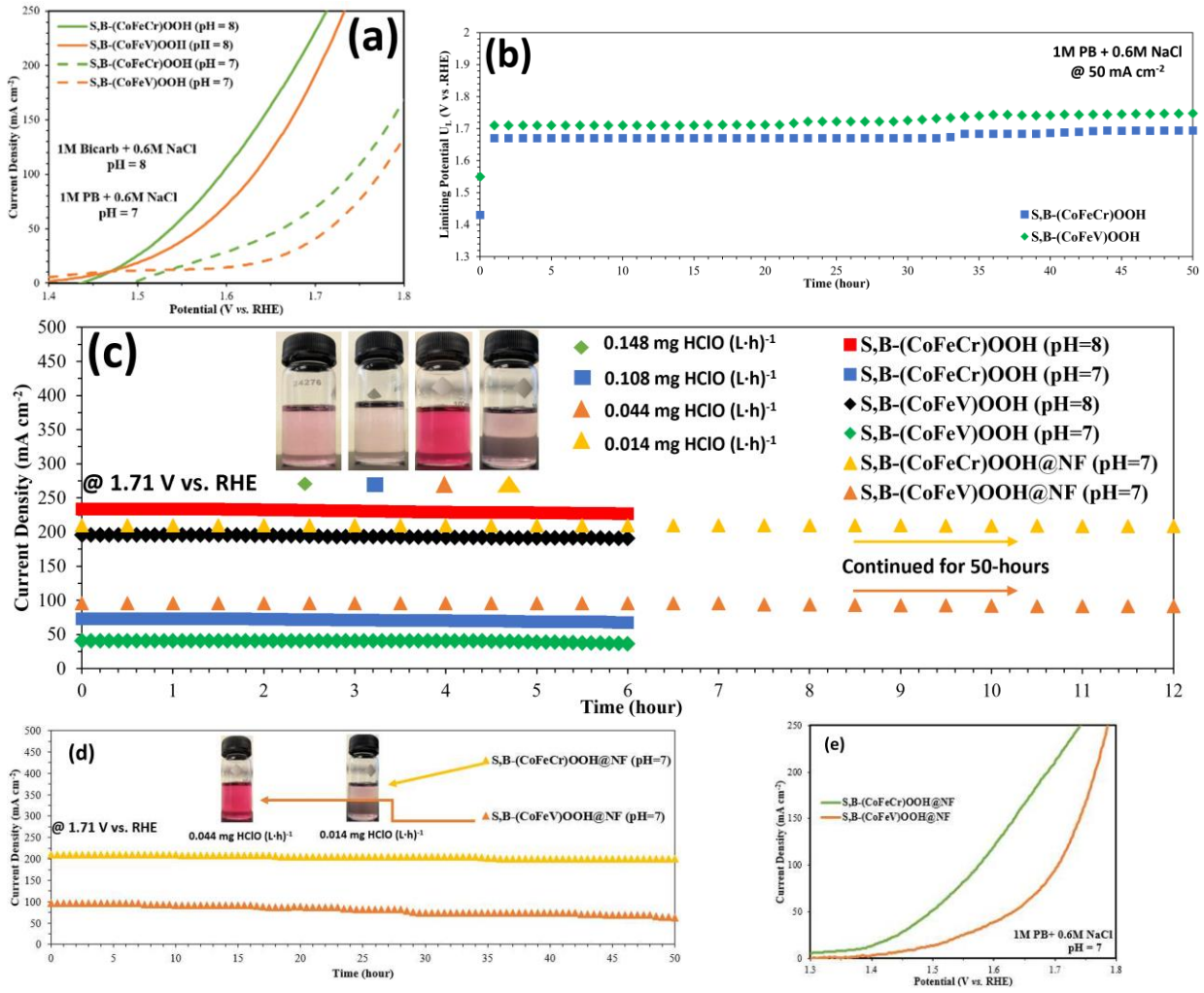

Figure 7. *(a) Polarization curves in near-neutral (1M + 0.6M NaCl; pH=8) and neutral saline pH (1M PB + 0.6M NaCl; pH=7) electrolytes and (b) chronoamperometry (CA) at 50 mA cm^{-2} in neutral saline electrolyte for the two S,B-codoped ternary oxyhydroxide catalysts. (c) Chronopotentiometry (CP) testing at 1.71 V (vs. RHE) for S,B-(CoFeCr)OOH and S,B-(CoFeV)OOH in near-neutral and neutral saline electrolytes using GCE and NF as substrates. Inset images of vials and corresponding CER product (i.e., HClO) evolution rate was determined through the DPD method at the end of the respective CP testing. (d) Full CP plot of both S,B-codoped oxyhydroxides deposited on NF evaluated under 50-hours and (e) polarization curves of S,B-(CoFe(ETM)OOH@NF in neutral saline environment.*

4. CONCLUSION

We have successfully synthesized S,B-codoped core-shell type CoFe(ETM) amorphous oxyhydroxide through a facile 2-step solution combustion synthesis-wet chemistry doping synthesis strategy. The optimum S,B-codoped ternary oxyhydroxides showed great enhancements in intrinsic catalytic kinetics (Tafel slopes), performance (overpotential), larger ECSA, hydrophilicity, and stability at high current density in both alkaline (1M KOH), near-neutral (1M Bicarbonate), and neutral (1M PB) pH saline (0.6M NaCl) electrolytes. We have fine-tuned the developed electrocatalysts towards enhanced water dissociation kinetics in neutral pH environments and attempted intrinsic CER suppression mechanisms atop the oxyhydroxide that also contribute towards an enhanced OER performance. S,B-(CoFeCr)OOH attained 172 mV overpotential at 10 mA cm^{-2} and a Tafel slope of 45.3 mV/dec (164 mV and 34 mV/dec when deposited on metallic NF substrate) in alkaline saline water. We further tested the developed catalysts for 50 hours of chronopotentiometry at 1.71 V (vs. RHE) to induce CER and investigate their CER suppression character. Higher CER suppression for the Cr analogue was attributed to stronger localized $Cr^{\delta+}(OOH)^{\delta-}$ bonds which activates stronger electrostatic shielding from anionic Cl^{-}. A multitude of textural, chemical and electrochemical characterizations were undertaken to probe and investigate the developed electrocatalysts and offer explanation on the achieved performances.

REFERENCES

1. Hosseini, S. E.; Wahid, M. A., Hydrogen production from renewable and sustainable energy resources: Promising green energy carrier for clean development. *Renewable and Sustainable Energy Reviews* **2016,** *57*, 850-866.

2. Nikolaidis, P.; Poullikkas, A., A comparative overview of hydrogen production processes. *Renewable and Sustainable Energy Reviews* **2017,** *67*, 597-611.

3. Pellow, M. A.; Emmott, C. J. M.; Barnhart, C. J.; Benson, S. M., Hydrogen or batteries for grid storage? A net energy analysis. *Energy & Environmental Science* **2015,** *8* (7), 1938-1952.

4. Hinicio, L., L., Fraile, Altmann, Barth, . . . Vanhoudt. Fuel Cells and Hydrogen 2 Joint Undertaking https://op.europa.eu/en/publication-detail/-/publication/9df9aa86-d60a-11e5-a4b5-01aa75ed71a1.

5. Gielen, D.; Boshell, F.; Saygin, D.; Bazilian, M. D.; Wagner, N.; Gorini, R., The role of renewable energy in the global energy transformation. *Energy Strategy Reviews* **2019,** *24*, 38-50.

6. Bo, X.; Li, Y.; Chen, X.; Zhao, C., High valence chromium regulated cobalt-iron-hydroxide for enhanced water oxidation. *Journal of Power Sources* **2018,** *402*, 381-387.

7. Park, S.; Shao, Y.; Liu, J.; Wang, Y., Oxygen electrocatalysts for water electrolyzers and reversible fuel cells: status and perspective. *Energy & Environmental Science* **2012,** *5* (11), 9331-9344.

8. Khatun, S.; Hirani, H.; Roy, P., Seawater electrocatalysis: activity and selectivity. *Journal of Materials Chemistry A* **2021**.

9. Lu, X.; Zhao, C., Electrodeposition of hierarchically structured three-dimensional nickel–iron electrodes for efficient oxygen evolution at high current densities. *Nature Communications* **2015,** *6* (1), 6616.

10. Godínez-Salomón, F.; Albiter, L.; Alia, S. M.; Pivovar, B. S.; Camacho-Forero, L. E.; Balbuena, P. B.; Mendoza-Cruz, R.; Arellano-Jimenez, M. J.; Rhodes, C. P., Self-

Supported Hydrous Iridium–Nickel Oxide Two-Dimensional Nanoframes for High Activity Oxygen Evolution Electrocatalysts. *ACS Catalysis* **2018,** *8* (11), 10498-10520.

11. Wu, T.; Sun, S.; Song, J.; Xi, S.; Du, Y.; Chen, B.; Sasangka, W. A.; Liao, H.; Gan, C. L.; Scherer, G. G.; Zeng, L.; Wang, H.; Li, H.; Grimaud, A.; Xu, Z. J., Iron-facilitated dynamic active-site generation on spinel CoAl2O4 with self-termination of surface reconstruction for water oxidation. *Nature Catalysis* **2019,** *2* (9), 763-772.

12. Bo, X.; Li, Y.; Chen, X.; Zhao, C., Operando Raman Spectroscopy Reveals Cr-Induced-Phase Reconstruction of NiFe and CoFe Oxyhydroxides for Enhanced Electrocatalytic Water Oxidation. *Chemistry of Materials* **2020,** *32* (10), 4303-4311.

13. Liu, D.; Ai, H.; Li, J.; Fang, M.; Chen, M.; Liu, D.; Du, X.; Zhou, P.; Li, F.; Lo, K. H.; Tang, Y.; Chen, S.; Wang, L.; Xing, G.; Pan, H., Surface Reconstruction and Phase Transition on Vanadium–Cobalt–Iron Trimetal Nitrides to Form Active Oxyhydroxide for Enhanced Electrocatalytic Water Oxidation. *Advanced Energy Materials* **2020,** *10* (45), 2002464.

14. Lukowski, M. A.; Daniel, A. S.; Meng, F.; Forticaux, A.; Li, L.; Jin, S., Enhanced Hydrogen Evolution Catalysis from Chemically Exfoliated Metallic MoS2 Nanosheets. *Journal of the American Chemical Society* **2013,** *135* (28), 10274-10277.

15. Hong, Y.-R.; Mhin, S.; Kim, K.-M.; Han, W.-S.; Choi, H.; Ali, G.; Chung, K. Y.; Lee, H. J.; Moon, S.-I.; Dutta, S.; Sun, S.; Jung, Y.-G.; Song, T.; Han, H., Electrochemically activated cobalt nickel sulfide for an efficient oxygen evolution reaction: partial amorphization and phase control. *Journal of Materials Chemistry A* **2019,** *7* (8), 3592-3602.

16. Li, Y.; Dong, Z.; Jiao, L., Multifunctional Transition Metal-Based Phosphides in Energy-Related Electrocatalysis. *Advanced Energy Materials* **2020,** *10* (11), 1902104.

17. Gupta, S.; Forster, M.; Yadav, A.; Cowan, A. J.; Patel, N.; Patel, M., Highly Efficient and Selective Metal Oxy-Boride Electrocatalysts for Oxygen Evolution from Alkali and Saline Solutions. *ACS Applied Energy Materials* **2020,** *3* (8), 7619-7628.

18. Chunduri, A.; Gupta, S.; Patel, M.; Forster, M.; Cowan, A. J.; Patel, N., Alkaline Water Oxidation Using a Bimetallic Phospho-Boride Electrocatalyst. *ChemSusChem* **2020,** *13* (24), 6534-6540.

19. Long, X.; Li, J.; Xiao, S.; Yan, K.; Wang, Z.; Chen, H.; Yang, S., A Strongly Coupled Graphene and FeNi Double Hydroxide Hybrid as an Excellent Electrocatalyst for the

Oxygen Evolution Reaction. *Angewandte Chemie International Edition* **2014,** *53* (29), 7584-7588.

20. Peng, X.; Pi, C.; Zhang, X.; Li, S.; Huo, K.; Chu, P. K., Recent progress of transition metal nitrides for efficient electrocatalytic water splitting. *Sustainable Energy & Fuels* **2019,** *3* (2), 366-381.

21. Fu, G.; Lee, J.-M., Ternary metal sulfides for electrocatalytic energy conversion. *Journal of Materials Chemistry A* **2019,** *7* (16), 9386-9405.

22. Xie, L.; Zhang, R.; Cui, L.; Liu, D.; Hao, S.; Ma, Y.; Du, G.; Asiri, A. M.; Sun, X., High-Performance Electrolytic Oxygen Evolution in Neutral Media Catalyzed by a Cobalt Phosphate Nanoarray. *Angewandte Chemie International Edition* **2017,** *56* (4), 1064-1068.

23. Duan, R.; Li, Y.; Gong, S.; Tong, Y.; Li, Z.; Qi, W., Hierarchical CoFe oxyhydroxides nanosheets and Co2P nanoparticles grown on Ni foam for overall water splitting. *Electrochimica Acta* **2020,** *360*, 136994.

24. Zhou, H.; Yu, F.; Zhu, Q.; Sun, J.; Qin, F.; Yu, L.; Bao, J.; Yu, Y.; Chen, S.; Ren, Z., Water splitting by electrolysis at high current densities under 1.6 volts. *Energy & Environmental Science* **2018,** *11* (10), 2858-2864.

25. Wang, Y.; Li, Y.; Ding, L.; Chen, Z.; Ong, A.; Lu, W.; Herng, T. S.; Li, X.; Ding, J., NiFe (sulfur)oxyhydroxide porous nanoclusters/Ni foam composite electrode drives a large-current-density oxygen evolution reaction with an ultra-low overpotential. *Journal of Materials Chemistry A* **2019,** *7* (32), 18816-18822.

26. Hu, Y.; Wang, Z.; Liu, W.; Xu, L.; Guan, M.; Huang, Y.; Zhao, Y.; Bao, J.; Li, H.-m., Novel Cobalt–Iron–Vanadium Layered Double Hydroxide Nanosheet Arrays for Superior Water Oxidation Performance. *ACS Sustainable Chemistry & Engineering* **2019,** *7* (19), 16828-16834.

27. Bajdich, M.; García-Mota, M.; Vojvodic, A.; Nørskov, J. K.; Bell, A. T., Theoretical Investigation of the Activity of Cobalt Oxides for the Electrochemical Oxidation of Water. *Journal of the American Chemical Society* **2013,** *135* (36), 13521-13530.

28. Zhang, B.; Wang, L.; Cao, Z.; Kozlov, S. M.; García de Arquer, F. P.; Dinh, C. T.; Li, J.; Wang, Z.; Zheng, X.; Zhang, L.; Wen, Y.; Voznyy, O.; Comin, R.; De Luna, P.; Regier, T.; Bi, W.; Alp, E. E.; Pao, C.-W.; Zheng, L.; Hu, Y.; Ji, Y.; Li, Y.; Zhang, Y.; Cavallo, L.; Peng, H.; Sargent, E. H., High-valence metals improve oxygen evolution

reaction performance by modulating 3d metal oxidation cycle energetics. *Nature Catalysis* **2020,** *3* (12), 985-992.

29. Dresselhaus, M. S.; Thomas, I. L., Alternative energy technologies. *Nature* **2001,** *414* (6861), 332-337.

30. Dionigi, F.; Reier, T.; Pawolek, Z.; Gliech, M.; Strasser, P., Design Criteria, Operating Conditions, and Nickel–Iron Hydroxide Catalyst Materials for Selective Seawater Electrolysis. *ChemSusChem* **2016,** *9* (9), 962-972.

31. Kirk, D. W.; Ledas, A. E., Precipitate formation during sea water electrolysis. *International Journal of Hydrogen Energy* **1982,** *7* (12), 925-932.

32. Tong, W.; Forster, M.; Dionigi, F.; Dresp, S.; Sadeghi Erami, R.; Strasser, P.; Cowan, A. J.; Farràs, P., Electrolysis of low-grade and saline surface water. *Nature Energy* **2020,** *5* (5), 367-377.

33. Hu, X.; Zhang, S.; Sun, J.; Yu, L.; Qian, X.; Hu, R.; Wang, Y.; Zhao, H.; Zhu, J., 2D Fe-containing cobalt phosphide/cobalt oxide lateral heterostructure with enhanced activity for oxygen evolution reaction. *Nano Energy* **2019,** *56*, 109-117.

34. Yu, F.; Zhou, H.; Zhu, Z.; Sun, J.; He, R.; Bao, J.; ... & Ren, Z., Three-dimensional nanoporous iron nitride film as an efficient electrocatalyst for water oxidation. *ACS Catalysis* **2017,** *7* (3), 2052-2057.

35. Hongyan, x.; Hai, Z.; Diwu, J.; Zhang, Q.; Gao, L.; Cui, D.; Zang, J.; Liu, J.; Xue, C., Synthesis and Microwave Absorption Properties of Core-Shell Structured Co 3 O 4 -PANI Nanocomposites. *Journal of Nanomaterials* **2015,** *2015*, 1-8.

36. Srinet, G.; Sharma, S.; Kumar, M.; & Anshul, A., Structural and optical properties of Mg modified ZnO nanoparticles: An x-ray peak broadening analysis. *Physica E: Low-dimensional Systems and Nanostructures* **2021,** *125*, 114381.

37. Kuai, C.; Zhang, Y.; Han, L.; Xin, H. L.; Sun, C. J.; Nordlund, D.; ... & Lin, F., Creating compressive stress at the NiOOH/NiO interface for water oxidation. *Journal of Materials Chemistry A* **2020,** *8* (21), 8(21), 10747-10754.

38. Dionigi, F.; Zeng, Z.; Sinev, I.; Merzdorf, T.; Deshpande, S.; Lopez, M. B.; ... & Strasser, P., In-situ structure and catalytic mechanism of NiFe and CoFe layered double hydroxides during oxygen evolution. *Nature communications* **2020,** *11* (1), 1-10.

39. Tang, C.-W.; Wang, C.-B.; Chien, S.-H., Characterization of cobalt oxides studied by FT-IR, Raman, TPR and TG-MS. *Thermochimica Acta - THERMOCHIM ACTA* **2008,** *473*, 68-73.

40. Badreldin, A.; Abdel-Wahab, A.; & Balbuena, P. B., Local Surface Modulation Activates Metal Oxide Electrocatalyst for Hydrogen Evolution: Synthesis, Characterization, and DFT Study of Novel Black ZnO. *ACS Applied Energy Materials* **2020,** *3* (11), 10590-10599.

41. Liang, Q.; Zhong, L.; Du, C.; Zheng, Y.; Luo, Y.; Xu, J.; ... & Yan, Q., Mosaic-Structured Cobalt Nickel Thiophosphate Nanosheets Incorporated N-doped Carbon for Efficient and Stable Electrocatalytic Water Splitting. *Advanced Functional Materials* **2018,** *28* (43), 1805075.

42. Baserga, A.; Russo, V.; Di Fonzo, F.; Bailini, A.; Cattaneo, D.; Casari, C. S.; ... & Bottani, C. E., Nanostructured tungsten oxide with controlled properties: Synthesis and Raman characterization. *Thin Solid Films* **2007,** *515* (16), 6465-6469.

43. Xu, W.; Lu, Z.; Sun, X.; Jiang, L.; & Duan, X., Superwetting electrodes for gas-involving electrocatalysis. *Accounts of chemical research* **2018,** *51* (7), 1590-1598.

44. Liu, G.; He, D.; Yao, R.; Zhao, Y.; & Li, J., Amorphous NiFeB nanoparticles realizing highly active and stable oxygen evolving reaction for water splitting. *Nano Research* **2018,** *11* (3), 1664-1675.

45. Exner, K. S.; & Over, H., Kinetics of electrocatalytic reactions from first-principles: a critical comparison with the ab initio thermodynamics approach. *Accounts of chemical research* **2017,** *50* (5), 1240-1247.

46. Wang, J.; Zhang, W.; Zheng, Z.; Liu, J.; Yu, C.; Chen, Y.; & Ma, K., Dendritic core-shell Ni@ Ni (Fe) OOH metal/metal oxyhydroxide electrode for efficient oxygen evolution reaction. *Applied Surface Science* **2019,** *469*, 731-738.

47. Yu, L.; Wu, L.; McElhenny, B.; Song, S.; Luo, D.; Zhang, F.; ... & Ren, Z., Ultrafast room-temperature synthesis of porous S-doped Ni/Fe (oxy) hydroxide electrodes for oxygen evolution catalysis in seawater splitting. *Energy & Environmental Science* **2020,** *13* (10), 3439-3446.

48. Hu, Y.; Wang, Z.; Liu, W.; Xu, L.; Guan, M.; Huang, Y.; ... & Li, H. M., Novel Cobalt–Iron–Vanadium Layered Double Hydroxide Nanosheet Arrays for Superior Water Oxidation Performance. *ACS Sustainable Chemistry & Engineering* **2019,** *7* (19), 16828-16834.

49. Xiao, Y.; Hu, C.; & Cao, M., High lithium storage capacity and rate capability achieved by mesoporous Co3O4 hierarchical nanobundles. *Journal of Power Sources* **2014,** *247*, 49-56.

50. Di, J.; Zhu, H.; Xia, J.; Bao, J.; Zhang, P.; Yang, S. Z.; ... & Dai, S., High-performance electrolytic oxygen evolution with a seamless armor core–shell FeCoNi oxynitride. *Nanoscale* **2019,** *11* (15), 7239-7246.

51. Liu, S.; Zhu, J.; Sun, M.; Ma, Z.; Hu, K.; Nakajima, T.; Liu, X.; Schmuki, P.; Wang, L., Promoting the hydrogen evolution reaction through oxygen vacancies and phase transformation engineering on layered double hydroxide nanosheets. *Journal of Materials Chemistry A* **2020,** *8* (5), 2490-2497.

52. Bazuev, G. V.; Tyutyunnik, A. P.; Kuznetsov, M. V.; & Samigullina, R. P., Apatite-Like Complex Oxides in the Ca–Cr–Cu–O System: Synthesis, Crystal Structure, XPS and Magnetic Study. *European Journal of Inorganic Chemistry* **2016,** *2016* (34), 5340-5346.

53. Al-Mamun, M.; Zhu, Z.; Yin, H.; Su, X.; Zhang, H.; Liu, P.; Yang, H.; Wang, D.; Tang, Z.; Wang, Y.; Zhao, H., The surface sulfur doping induced enhanced performance of cobalt catalysts in oxygen evolution reactions. *Chemical Communications* **2016,** *52* (60), 9450-9453.

54. Khoo, S. Y.; Miao, J.; Yang, H. B.; He, Z.; Leong, K. C.; Liu, B.; Tan, T. T. Y., One-Step Hydrothermal Tailoring of NiCo2S4 Nanostructures on Conducting Oxide Substrates as an Efficient Counter Electrode in Dye-Sensitized Solar Cells. *Advanced Materials Interfaces* **2015,** *2* (18), 1500384.

55. Sartz, W. E.; Wynne, K. J.; Hercules, D. M., X-ray photoelectron spectroscopic investigation of Group VIA elements. *Analytical Chemistry* **1971,** *43* (13), 1884-1887.

56. Ahmadi, M. A., Chapter Six - Chemical Flooding. In *Fundamentals of Enhanced Oil and Gas Recovery from Conventional and Unconventional Reservoirs*, Bahadori, A., Ed. Gulf Professional Publishing: 2018; pp 187-205.

57. Jiang, N.; You, B.; Sheng, M.; & Sun, Y., Electrodeposited cobalt-phosphorous-derived films as competent bifunctional catalysts for overall water splitting. *Angewandte Chemie* **2015,** *127* (21), 6349-6352.

58. Masa, J.; Weide, P.; Peeters, D.; Sinev, I.; Xia, W.; Sun, Z.; ... & Schuhmann, W., Amorphous cobalt boride (Co2B) as a highly efficient nonprecious catalyst for electrochemical water splitting: oxygen and hydrogen evolution. *Advanced Energy Materials* **2016,** *6* (6), 1502313.

59. Li, Y.; Huang, B.; Sun, Y.; Luo, M.; Yang, Y.; Qin, Y.; ... & Guo, S., Multimetal borides nanochains as efficient electrocatalysts for overall water splitting. *Small* **2019,** *15* (1), 1804212.

60. Wang, T.; Nam, G.; Jin, Y.; Wang, X.; Ren, P.; Kim, M. G.; ... & Cho, J., NiFe (Oxy) hydroxides derived from NiFe disulfides as an efficient oxygen evolution catalyst for rechargeable Zn–air batteries: the effect of surface S residues. *Advanced Materials* **2018,** *30* (27), 1800757.

61. Zhang, T.; Du, J.; Xi, P.; & Xu, C., Hybrids of cobalt/iron phosphides derived from bimetal–organic frameworks as highly efficient electrocatalysts for oxygen evolution reaction. *ACS applied materials & interfaces* **2017,** *9* (1), 362-370.

62. Dong, Z.; Zhang, W.; Xiao, Y.; Wang, Y.; Luan, C.; Qin, C.; ... & Zhang, X., One-Pot-Synthesized CoFe-Glycerate Hollow Spheres with Rich Oxyhydroxides for Efficient Oxygen Evolution Reaction. *ACS Sustainable Chemistry & Engineering* **2020,** *8* (14), 5464-547.

63. Cai, Z.; Li, L.; Zhang, Y.; Yang, Z.; Yang, J.; Guo, Y.; & Guo, L., Amorphous Nanocages of Cu-Ni-Fe Hydr (oxy) oxide Prepared by Photocorrosion For Highly Efficient Oxygen Evolution. *Angewandte Chemie International Edition* **2019,** *58* (13), 4189-4194.

64. Hu, X.; Zhang, S.; Sun, J.; Yu, L.; Qian, X.; Hu, R.; ... & Zhu, J., 2D Fe-containing cobalt phosphide/cobalt oxide lateral heterostructure with enhanced activity for oxygen evolution reaction. *Nano Energy* **2019,** *56*, 109-117.

65. Song, F.; Busch, M. M.; Lassalle-Kaiser, B.; Hsu, C. S.; Petkucheva, E.; Bensimon, M.; ... & Hu, X., An unconventional iron nickel catalyst for the oxygen evolution reaction. *ACS central science* **2019,** *5* (3), 558-568.

66. Liu, D.; Ai, H.; Li, J.; Fang, M.; Chen, M.; Liu, D.; ... & Pan, H., Surface Reconstruction and Phase Transition on Vanadium–Cobalt–Iron Trimetal Nitrides to Form Active Oxyhydroxide for Enhanced Electrocatalytic Water Oxidation. *Advanced Energy Materials* **2020,** *10* (45), 2002464.

67. Chunduri, A.; Gupta, S.; Patel, M.; Forster, M.; Cowan, A. J.; & Patel, N., Synergistic effect in bi-metallic phospho-boride electrocatalyst for alkaline water oxidation. *Chemsuschem* **2020**.

68. Lu, W.; Liu, T.; Xie, L.; Tang, C.; Liu, D.; Hao, S.; ... & Sun, X., In Situ Derived Co□ B Nanoarray: A High-Efficiency and Durable 3D Bifunctional Electrocatalyst for Overall Alkaline Water Splitting. *Small* **2017,** *13* (32), 1700805.

69. Seh, Z. W.; Kibsgaard, J.; Dickens, C. F.; Chorkendorff, I. B.; Nørskov, J. K.; & Jaramillo, T. F., Combining theory and experiment in electrocatalysis: Insights into materials design. *Science* **2017,** *355* (6321).

70. Nie, L.; Mei, D.; Xiong, H.; Peng, B.; Ren, Z.; Hernandez, X. I. P.; ... & Wang, Y., Activation of surface lattice oxygen in single-atom Pt/CeO2 for low-temperature CO oxidation. *Science* **2017,** *358* (6369), 1419-1423.

71. Huang, Z. F.; Song, J.; Du, Y.; Xi, S.; Dou, S.; Nsanzimana, J. M. V.; ... & Wang, X., Chemical and structural origin of lattice oxygen oxidation in Co–Zn oxyhydroxide oxygen evolution electrocatalysts. *Nature Energy* **2019,** *4* (4), 329-338.

72. Li, P.; Zhao, R.; Chen, H.; Wang, H.; Wei, P.; Huang, H.; Liu, Q.; Li, T.; Shi, X.; Zhang, Y.; Liu, M.; Sun, X., Recent Advances in the Development of Water Oxidation Electrocatalysts at Mild pH. *Small* **2019,** *15* (13), 1805103.

73. Cheng, F.; Feng, X.; Chen, X.; Lin, W.; Rong, J.; & Yang, W., Synergistic action of Co-Fe layered double hydroxide electrocatalyst and multiple ions of sea salt for efficient seawater oxidation at near-neutral pH. *Electrochimica Acta* **2017,** *251*, 336-343.

74. Gayen, P.; Saha, S.; & Ramani, V., Selective Seawater Splitting Using Pyrochlore Electrocatalyst. *ACS Applied Energy Materials* **2020,** *3* (4), 3978-3983.

75. Naito, T.; Shinagawa, T.; Nishimoto, T.; & Takanabe, K., Water Electrolysis in Saturated Phosphate Buffer at Neutral pH. *ChemSusChem* **2020,** *13* (22), 5921.

76. Obata, K.; van de Krol, R.; Schwarze, M.; Schomäcker, R.; & Abdi, F. F., In situ observation of pH change during water splitting in neutral pH conditions: impact of natural convection driven by buoyancy effects. *Energy & Environmental Science* **2020,** *13* (12), 5104-5116.

77. Pinkernell, U.; Nowack, B.; Gallard, H.; & Von Gunten, U., Methods for the photometric determination of reactive bromine and chlorine species with ABTS. *Water Research* **2000,** *34* (18), 4343-4350.